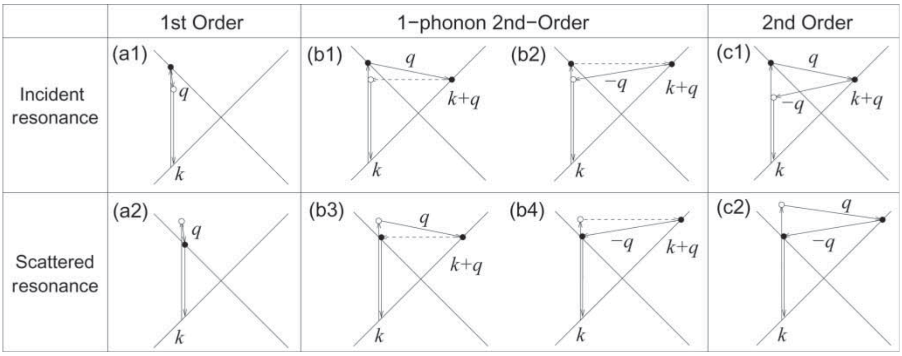

Figure 23. Schematic diagrams for (a1,a2) first-order and (b1–b4) one-phonon second-order, (c1,c2) two-phonon second-order, resonance Raman spectral processes for which the top diagrams refer to incident photon resonance conditions and the bottom diagrams refer to the scattered resonance conditions. For one-phonon, second-order transitions, one of the two scattering events is an elastic scattering event (dashed line). Resonance points are shown as solid circles [104,207–209]. Adapted with permission from R. Saito *et al.*, New Journal of Physics 5, p. 157, 2003 [209]. Copyright © (2003) by the Institute of Physics.

intermediate state back to k (see Figure 23(b) and (c)) [209]. This two-scattering amplitude process is expressed by perturbation theory in which the numerator of the resulting term consist of four scattering matrix elements (two for photon absorption and emission, and two for phonon emission or absorption), while the denominator of this term consists of three energy difference factors. If two of the three energy difference factors becomes zero, the scattering intensity becomes strongly enhanced by each of these factors. We call a process containing two resonance denominators double resonance (DR) Raman scattering [104,174,207,210,211]. The G′-band of mono-layer graphene represents a resonance Raman spectral feature for an iTO phonon mode near the K point which is resonant for each of the three scattering processes.

2.8.5. *Dispersive behavior of the phonon energy in DR Raman processes*

An important aspect of the DR Raman spectra is that the observed phonon energy changes by changing the laser excitation energy, which gives rise to a dispersive behavior of the scattered phonon. Since the electronic energy dispersion of the π and π^* bands is linear in k as measured from the K (K') point in the 2D BZ of graphene, a special k value is selected on an equi-energy line for a given laser energy (E_{laser}). In order to satisfy energy–momentum conservation for the DR scattering from k to $k - q$ and from $k - q$ to k, the phonon momentum q is selected by the circles near the K point shown in Fig. 23(c). When we calculate the phonon density of states for this DR process, the DR wave vector $q_{\text{DR}} \approx 2k$ for a phonon frequency $\omega(q)$ is selected [104,207]. Thus by changing the photon energy, we can probe the phonon energy along the phonon energy dispersion [174,210,212]. The D- (G′-) band frequency is 1350 (2700) cm^{-1} for $E_{\text{laser}} = 2.41$ eV and the D-(G’)-band frequency increases by 53 (106) cm^{-1} by changing E_{laser} by 1 eV [213]. In the case of SWNTs, the selection of q_{DR} becomes more selective because of the 1D character of q_{DR}, which is the reason why a sharp D-band spectral feature occurs in the case of SWNTs [210,211]. The pioneering work on the variation of the G′-band peak frequency with laser excitation energy was first studied by Vidano *et al.* [214,215] and by Baranov *et al.* [207].

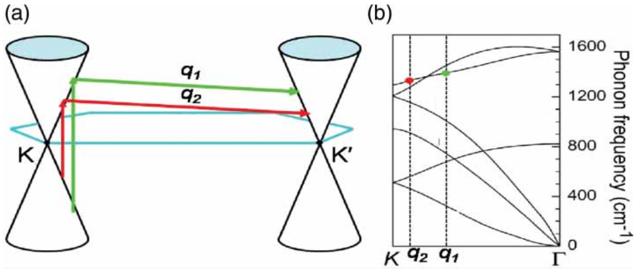

Figure 24. (a) The schematic diagram shows the light-induced e–h formation and the one electron–one phonon scattering event taking place in the DR process with two different excitation laser energies (associated with phonon wave vectors q_1 and q_2, respectively), which are indicated by the gray and black arrows, respectively. The two events in the DR process can occur in either order in time. (b) The phonon dispersion in graphene is shown where the phonon wavevector q that fulfills the DR requirements for each E_{laser} value in (a) is also indicated in terms of the phonon wavevectors q_1 and q_2 (see text). Reprinted figure with permission from A. Jorio *et al.* Spectroscopy in Graphene Related Systems, 2010 [1]. Copyright © Wiley–VCH Verlag GombH & Co. KGaA.

2.8.6. *The inter-valley double resonance Raman scattering processes*

When a photon with a given energy is incident on mono-layer graphene, it will excite an electron from the valence band to the conduction band vertically in momentum space (vertical arrows in Figure 24(a)). Since the graphene energy band does not have an energy gap, we always have an electron with wavevector k for any E_{laser} value which satisfies energy conservation $E_{\text{laser}} = E^{c}(k) - E^{v}(k)$. In the single-resonance Raman process, a zone center ($q = 0$) phonon is created or destroyed by coupling with the excited electron or hole, and the e–h recombination generates the Raman shifted photon.

In contrast, the photo-excited electron at k can be scattered by emitting a phonon with wave vector q to a state at $k - q$, as shown by the quasi-horizontal arrows in Figure 24(a). The phonon emission in Figure 24(a) corresponds to an inter-valley scattering process in which the phonon q vector connects two energy bands at the K and K' points of the BZ. If there is a phonon in the vibrational structure of graphene with the wavevector q and phonon energy E_q so that this photon can connect the two conduction electronic states, then this phonon scattering process will be resonant. The DR process (involving both electron–photon and el–ph scattering, shown in Figure 24(a)) will then take place.

2.8.7. *Forward and backward scattering*

The slope of the energy dispersion $\partial E/\partial k$ is called the *group velocity*. When we consider only the direction of the group velocity for the initial k, there are two possibilities for the scattered $k - q$ states, as shown in Figure 25, where each of the inter-valley (a,b) and intra-valley (c,d) scattering processes correspond to backward (a,c) and forward (b,d) scattering. Here the backward (forward) scattering means that the direction of the group velocity does (does not) change after scattering. The corresponding q vectors for inter-valley scattering are given by (see Figure 26)

$$q = K + q_{\text{DR}} = K + k + k' \approx K + 2k \quad \text{(backward scattering)}, \tag{11}$$

$$q = K + q_{\text{DR}} = K + k - k' \approx K \quad \text{(forward scattering)}, \tag{12}$$

where K is the magnitude of the reciprocal lattice vector that connects K and K', and k (k') here is measured from the K (K') point, which means that the double resonance wave vector q_{DR} is the

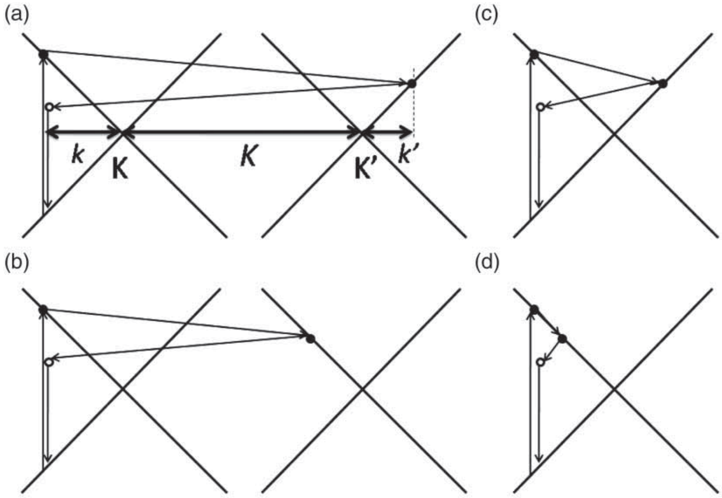

Figure 25. The full DR Stokes Raman processes for inter-valley (a,b) and intra-valley (c,d) scattering. Here (a,c) relates to the backward scattering process with $q_{\rm DR} = k + k'$ and (b,d) relates to the forward scattering process with $q_{\rm DR} = k - k'$, with k and k' measured from the K point. The reciprocal lattice vector K is the distance between the K and K' points, k (k') is the distance of the resonant states from K (K'), as defined in (a). Reprinted figure with permission from A. Jorio *et al.* Spectroscopy in Graphene Related Systems, 2010 [1]. Copyright © Wiley–VCH Verlag GombH & Co. KGaA.

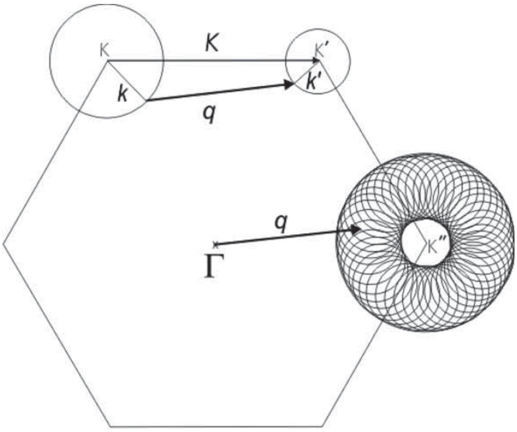

Figure 26. One of the possible DR Stokes Raman processes involving the emission of a phonon with wavevector $-\mathbf{q}$. The set of all phonon wavevectors $\mathbf{q}$ which are related to transitions from points on the two circles around K and K' gives rise to the collection of small circles around the K'' point obeying the vector sum rule $\mathbf{q} = \mathbf{K} - \mathbf{k} + \mathbf{k}'$ (here we neglect the trigonal warping effect). Note that this collection of circles is confined to a region between the two circles with radii $q_{\rm DR} = k + k' \approx 2k$ and $q_{\rm DR} = k - k' \approx 0$. The differences between the radii of the circles around K and K' and thus the radius of the inner circle around K'' are actually small in magnitude and are here artificially enlarged for clarity in presenting the concepts of the double resonance process. Adapted with permission from L.G. Cançado *et al.*, Physical Review B 66, p. 35415, 2002 [216]. Copyright © (2002) by the American Physical Society.

phonon wavevector distance linking the K and K' points. In the case of intra-valley scattering, we just put $K = 0$ into Equations (11) and (12). Since the phonon energy is usually small compared to the excited electronic energy levels, $k \approx k'$, these two double resonance conditions approach $q_{\mathrm{DR}} = 2k$ and $q_{\mathrm{DR}} = 0$ (as is commonly used in the literature [114,172,210]).

2.8.8. *DR* q *circles in 2D graphene*

The picture discussed up to now is not the full story because graphene is a 2D material. For a given laser energy, not only is the e–h excitation process shown in Figure 24 resonant, but any similar process on a circle in these cones defined by E_{laser} (see Figure 26) is also resonant. Furthermore, the mechanism of DR is actually satisfied by any phonon whose wavevector connects two points on two circles around the K and K' points, as shown in Figure 26 [216]. (In constructing this figure, we neglect the trigonal warping effect of the constant energy surface of graphene for simplicity). A phonon with wavevector q connects two points along the circles with radii k and k' around the K and K' points, respectively, where the difference between k and k' (for $k \neq k'$) comes from the energy loss from the electron to the phonon.[15] By translating the vector q to the Γ point, and considering all possible initial and final states around the K and K' points, the doughnut-like figure shown in Figure 26 is generated [216]. Therefore, there is a large set of q vectors fulfilling the DR condition. However, there is also a high density of phonon wavevectors $\mathbf{q}$ satisfying the DR mechanism for which the end points of the wavevectors measured from the Γ point are on the inner and outer circles of the “doughnut” in Figure 26. Therefore, the radii of the inner and outer circles around K'' (see Figure 26) are, respectively, $k - k'$ and $k + k'$. Exactly as given by the 1D model (Equations (11) and (12)), these wavevectors correspond to the phonons associated with the singularities in the density of $\mathbf{q}$ vectors that fulfill the DR requirements, and these special wavevectors in Figure 26 are expected to make a significantly larger contribution to the second-order Raman scattering process. However, for a full description and lineshape analysis, it is important to consider the 2D model, which seems to generate the asymmetric lineshape that is observed for the 2450 cm^{-1} G$'$-band feature.

Finally, Figure 24 shows that, if E_{laser} is changed, then the specific wavevector q and phonon energy E_q that will fulfill the DR conditions will also change. This effect gives rise to the dispersive nature of the G$'$-band, which comes from an *inter-valley* DR Raman process involving an electron with wave vector k in the vicinity of the K point and two iTO phonons with wave vectors $q_{\mathrm{DR}} \approx 2k$, where both k and q_{DR} are measured from the K point.

To analyze experimental data for graphene in Figure 27 one has to consider the electron and phonon dispersion of a graphene mono-layer. Near the K point, the electron and phonon dispersions can be approximated by the linear relations $E(k) = \hbar v_{\mathrm{F}} k$ and $E(q_{\mathrm{DR}}) = \hbar v_{\mathrm{ph}} q_{\mathrm{DR}}$, respectively, where $v_{\mathrm{F}} = \partial E(k)/\partial k$ and $v_{\mathrm{ph}} = \partial E(q)/\partial q$ are the electron and phonon velocities near the K point, respectively (in which v_{F} is usually called the Fermi velocity, $v_{\mathrm{F}} \sim 10^6$ m/s) for graphene. We denote the electron (phonon) wave vector by k (q_{DR}) which is measured with respect to the K point, so that the conditions for the DR Raman effect are given by [1]

$$\begin{aligned} E_{\mathrm{laser}} &= 2v_{\mathrm{F}}k, \\ E_{\mathrm{ph}} &= v_{\mathrm{ph}} q_{\mathrm{DR}}, \\ q_{\mathrm{DR}} &= k \pm k', \end{aligned} \tag{13}$$

where E_{laser} and E_{ph} are, respectively, the laser and phonon energies, and k' is the scattered electron wave vector near the K' point in the graphene BZ. It is important to remember that we are dealing here with combination modes, so that the observed E_{ph} has to reflect this combination. For example, for the G$'$-band, the observed G$'$-band energy is given by $E_{\mathrm{G}'} = 2E_{\mathrm{ph}}$, where E_{ph} is the energy for the iTO phonon mode at q_{DR}.[16] Making another commonly used approximation in Equation (13), i.e., $q_{\mathrm{DR}} = k + k' \approx 2k$, then $E_{\mathrm{G}'}$ can be written as [1]

$$E_{\mathrm{G}'} = 2\frac{v_{\mathrm{ph}}}{v_{\mathrm{F}}}E_{\mathrm{laser}}. \tag{14}$$

A drawback in using the DR Raman features to define the electron and phonon dispersion relations is that the measured values depend on both v_{ph} and v_{F}, and one has to be known in order to obtain the other. In addition to this problem, the physics of the phonon dispersion for graphene near the K point is rather complex due to the Kohn anomaly, and the KA also occurs for phonons at $q \to K$ (see Section 2.7). The high frequency of the iTO phonon when combined with the KA near the K point are together responsible for the strong dispersive behavior observed for $\omega_{\mathrm{G}'}$. The exact values for v_{ph} and v_{F} are still under debate since they also depend on the complex physics of many-body effects [112,194,217–220]. This is one area where more work for future research is needed.

2.8.9. *Dispersive behavior of the G′- and G*-band*

Since both G* and G′ features in Figure 27 are due to double resonance processes, both Raman features show dispersion with E_{laser}, but with quite different characteristics. So far, we explained that there are two possibilities for selecting q while satisfying the double resonance condition: $q_{\mathrm{DR}} \approx 2k$ and 0. The condition for $q_{\mathrm{DR}} \approx 0$ will or no select a phonon frequency at $q = 0$ measured from the K point, and these q_{DR} show weak dispersion even though the signal is due to a DR Raman spectra. Figure 27(a) shows the Raman spectra in the region of both the G* ($\sim 2450\,\mathrm{cm}^{-1}$) and G′ ($\sim 2700\,\mathrm{cm}^{-1}$) bands for different laser excitation energies. Also the G*-band can either be explained by the $q \approx 0$ DR relation [221] or by the $q \approx 2k$ relation applied to an *inter-valley* process [213], but involving two different phonons in each case. Figure 27(b) shows the G′ and G*

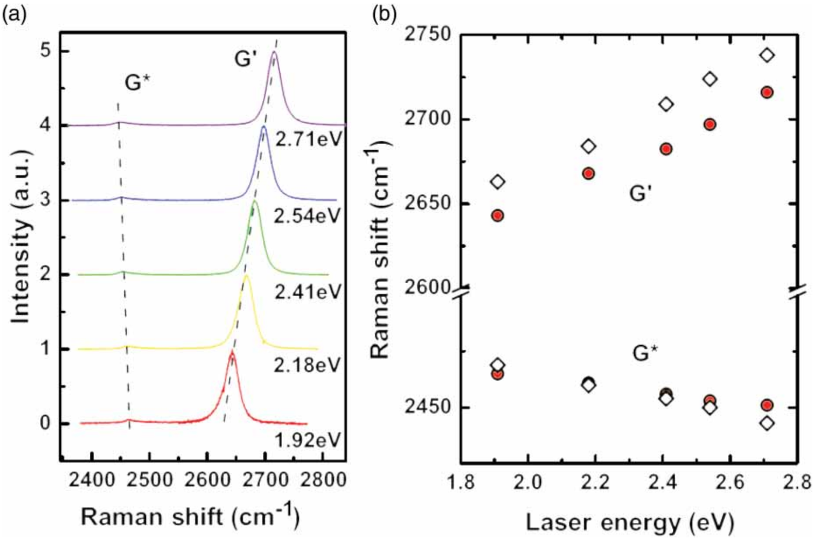

Figure 27. (a) Raman spectra of the G′ and the G*-bands of mono-layer graphene for 1.92, 2.18, 2.41, 2.54 and 2.71 eV laser excitation energy. (b) Dependence of $\omega_{\mathrm{G}'}$ and ω_{G^*} on E_{laser}. The circles correspond to the graphene data and the lozenges correspond to data for turbostratic graphite. Adapted with permission from D. Mafra *et al.*, Physical Review B, 76, p. 233407, 2007 [213]. Copyright © (2007) by the American Physical Society.

frequencies $\omega_{G'}$ and ω_{G^*} as a function of E_{laser} for graphene and turbostratic graphite (for which the stacking between graphene layers is random). The G′-band in Figure 27 exhibits a highly dispersive behavior with $(\partial\omega_{G'}/\partial E_{\text{laser}}) \simeq 88\,\text{cm}^{-1}$/eV for mono-layer graphene, $95\,\text{cm}^{-1}$/eV for turbostratic graphite [213] and $106\,\text{cm}^{-1}$/eV for carbon nanotubes (see Figure 27 and [222]). The G*-band feature exhibits a much less pronounced dispersion than the G′-band, and of opposite sign, with $(\partial\omega_{G^*}/\partial E_{\text{laser}}) \simeq -10$ to $-20\,\text{cm}^{-1}$/eV for both mono-layer and turbostratic graphite [208,213], and no dispersion is reported for carbon nanotubes [221]. It should be noted that a different interpretation to the origin of the G*-band is given in [131,223], which together with [221] identified the origin of the $2450\,\text{cm}^{-1}$ peak with the overtone of the $1225\,\text{cm}^{-1}$ feature which has a peak in the phonon density of states for two phonons [223], while [224,225] assigned this feature to the combination modes iTA + iTO. As already stated, the $q_{\text{DR}} \approx 2k$ wavevector gives rise to the G′-band, while the $q_{\text{DR}} \approx 0$ wavevector gives rise to a DR feature coming from the iTO phonon very close to the K point. The $q_{\text{DR}} \approx 0$ processes are expected to be less intense than the $q_{\text{DR}} \approx 2k$ processes because the destructive interference condition is exactly satisfied for $q_{\text{DR}} = 0$ [208].

2.8.10. *Double resonance, overtone and combination modes*

The sp^2 carbons exhibit several combination modes and overtones, which are shown in Figure 28 for graphite whiskers as a function of frequency up to $7000\,\text{cm}^{-1}$ [226]. Basically all the branches in the phonon dispersion can be seen to have a combination and overtone Raman features which obey the DR condition [104,210]. Many of the peaks observed in the spectra of Figure 28 below $1650\,\text{cm}^{-1}$ are actually one-phonon bands activated by defects (see Section 4.3). Above $1650\,\text{cm}^{-1}$, the observed Raman features are all multiple-order combination modes and overtones, and here too some of the features in Figure 28 are also activated by defects.

As shown in Figure 28, the DR peaks change frequency with changing E_{laser}, and they can be fitted onto the phonon dispersion diagram shown in Figure 29 using DR theory. The data points displayed in Figure 29 all stand for the $q_{\text{DR}} \approx 2k$ DR backward resonance condition, those near Γ and K coming from intra-valley and inter-valley scattering processes, respectively. Actually, in the Raman spectra there are no characteristic features distinguishing peaks associated with the intra-valley scattering process from those associated with inter-valley scattering processes, or even features that distinguish between the $q_{\text{DR}} \approx 2k$ or $q_{\text{DR}} \approx 0$ resonance conditions. All we have in hand in analyzing actual Raman spectra is the E_{laser} dependence of each peak. Here, each peak has to fulfill one of the DR processes and to fit the predicted phonon dispersion relations. For example, the data points near the K point in Figure 29 that are assigned as the iTO+LA combination mode (TO+LA) could alternatively be assigned to a $q_{\text{DR}} \approx 0$ process, since this combination mode is weakly dispersive [221]. Supporting this assignment is the asymmetric (DR phonon-density-of-states-like shape) observed for this peak, and against this identification is the destructive interference working towards DR Raman processes at exactly $q = K$ [208]. The debate about the iTO + LA combination mode assignment near the K point remains for future clarification. Near the Γ point, the dispersive behavior is more clear and the assignment of the observed Raman features is on a more solid foundation [227].

2.9. ***Summary***

The power of Raman spectroscopy for studying carbon nanotubes is in particular revealed through exploitation of the resonance Raman effect, which is greatly enhanced by the singular density of electronic states of SWNTs and the resonant effect comes from the 1D confinement of the electronic states due to the small diameters of carbon nanotubes. Soon after the discovery of the

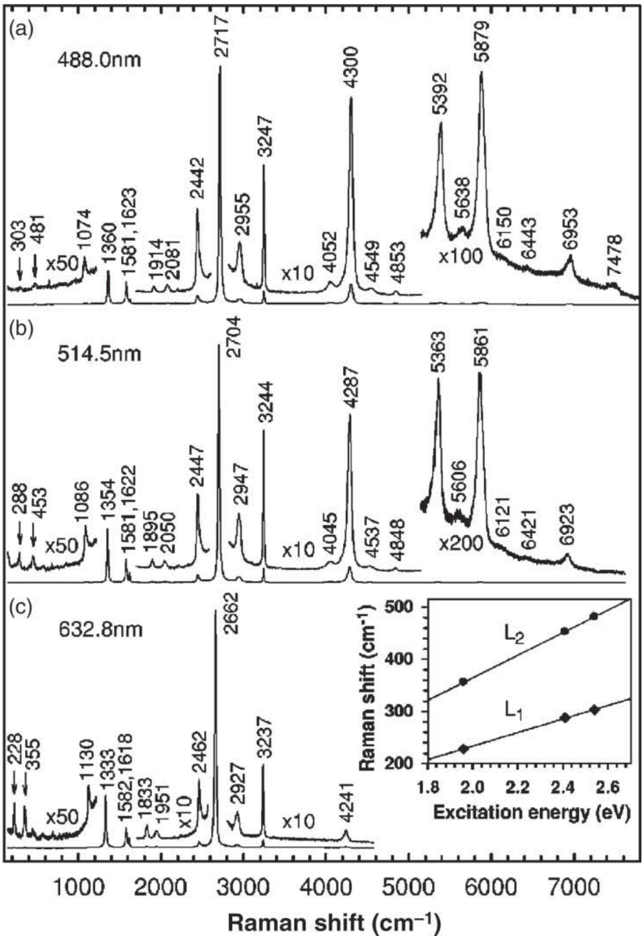

Figure 28. Raman spectra of graphite whiskers obtained at three different laser wavelengths (excitation energies) [226]. Note that some phonon frequencies vary with E_{laser} and some do not. Above 1650 cm^{-1} the observed Raman features are all multiple-order combination modes and overtones (see Figure 29), though some of the peaks observed below 1650 cm^{-1} are actually one-phonon bands activated by defects. The inset to (c) shows details of the peaks labeled by L_1 and L_2. The L_1 and L_2 peaks, which are dispersive, are explained theoretically by the defect activation of double-resonance one-phonon processes (see Section 2.8.10) involving the acoustic iTA and LA branches, respectively, as discussed in Ref. [210]. Adapted figure with permission from P.H. Tan *et al.*, Physical Review B 64, p. 214301, 2001 [226]. Copyright © (2001) by the American Physical Society.

resonance Raman effect in SWNTs [103], it was found that the resonance lineshape could be used to identify the nanotube structure, i.e., the chiral indices (n, m) [111], and to distinguish metallic from semiconducting SWNTs [128,228]. It is clear that most of the results achieved up to now have been developed for SWNTs, while the optics of graphene and nanoribbons is still at an early stage. This is the way it happened historically, and the knowledge developed in carbon nanotube science is now fostering an amazingly fast development of graphene photo-physics. It is expected that graphene photo-physics will follow a similar path of development that will reveal much new physics as this very fundamental field develops such as the understanding of the KA which helped to elucidate the phonon dispersion relation of graphite and all related sp^2 carbons.

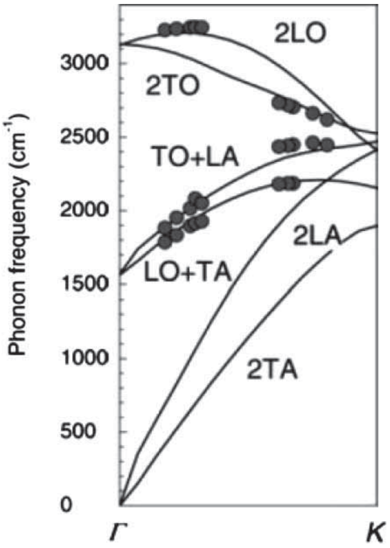

Figure 29. Two-phonon dispersion of graphite based on second-order double-resonance peaks in the Raman spectra (dark circles). Solid lines are dispersion curves from *ab initio* calculations considering combination modes and overtones associated with totally symmetric irreducible representations. Adapted figure with permission from J. Maultzsch *et al.*, Physical Review B 70, p. 155403, 2004 [208]. Copyright © (2004) by the American Physical Society.

3. Calculation method of resonance Raman spectra

Within the tight-binding approximation methods, we can calculate the Raman spectra and the Raman excitation profile of an (n, m) nanotube by considering the electron–photon, el–ph, exciton–photon and exciton–phonon interactions. In this section, the (n, m) dependence of the RBM and G-band intensities, spectral width and resonance window are directly compared with experiment. The exciton energy calculations can reproduce the E_{ii} energy within high accuracy. In Section 3, however, we do not mention the environmental effects (see Section 5.2.1) which are here comparatively considered here by experiment [229,230] and theory [231,232]. The electron–electron interaction and elastic scattering matrix elements [233] need to be developed further for obtaining the asymmetric shape of the BWF lines and the D- (G′-) band spectra, respectively. Using the established computer library, we can extend these calculations to consideration of the coherent phonon response of a nanotube [165]. In this section, we do not mention the polarization dependence of the Raman spectra, in which the screening effect (the so-called depolarization effect [234]) is important.

3.1. *Overview of calculations reviewed in this section*

In Section 3, we review the theoretical calculation of the resonance Raman spectra and exciton energy states for carbon nanotubes. The method used here for carbon nanotube calculations can also be applied to graphene Raman spectra, though we do not need to consider exciton states for graphene. Most of the quantitative comparisons are made in Section 3 with regard to resonance energy, Raman frequencies and spectral linewidths. In order to obtain the Raman intensity, we review the calculations of the excitonic (electronic) interaction matrix element for nanotubes (graphene). Since the derivations consist of many topics, each topic is first briefly mentioned in this subsection and is then described in more detail in the following subsections.

3.1.1. *Raman scattering and phonon energy dispersion*

In Raman spectroscopy studies of solids, we generally observe the phonon frequency at the center of the BZ (zone-center phonon). Other inelastic scattering techniques, such as inelastic neutron scattering [235,236], or inelastic X-ray scattering [208] or electron energy loss spectroscopy [237,238] provide measurements of the phonon dispersion inside the BZ, which we can reproduce theoretically [235,239] either by fitting force-constant calculations to experimental data or by first-principles calculations [32,240,241]. Graphene-related systems have a special electronic structure which allows the observation of phonons in the interior of the BZ by DR Raman spectroscopy. In Section 3.2, we mention how to obtain the phonon dispersion relations by force-constant models.

3.1.2. *Electronic energy bands*

Optical processes can be studied by Raman spectroscopy as well as by other techniques. If there is either a photo-absorption or a photo-emission process that couples the ground state to an excited state of an electron, then the amplitude of the phonon scattering process is greatly enhanced if the excited state is a real electronic state. This resonant process is known as resonance Raman spectroscopy. In order to obtain the resonance condition by which a given laser energy E_{laser} matches the transition energy of the actual electronic states, the electronic energy bands are calculated by a simple tight-binding method in Section 3.3 or by an extension of this method as given in Section 3.3.1 using the so-called extended tight-binding model. Angle-resolved photo-electron spectroscopy (ARPES) experiments [123–126] are especially relevant for providing information about the occupied electronic energy bands in graphene.

3.1.3. *The double resonance process*

While the most usual first-order Raman processes measure only zone center phonon modes, excited electron scattering processes may also take place involving phonons in the interior of the BZ. Such processes can become Raman allowed either by two phonon scattering processes, thus conserving momentum, or in the presence of a lattice defect, where the momentum conservation requirement can be broken. However, these are generally low probability processes. In graphene-related systems, however, such DR scattering processes become highly probable because of the so-called DR phenomena in graphene [104,207,210]. One resonant phenomenon is light absorption or emission, and the other resonant phenomenon is the scattering of the excited electron (or hole) by phonons. Here "resonant" means that the phonon brings the electron from one real state to another real state, which matches the energy and momentum transfer required for momentum and energy conservation.

3.1.4. *Electron–photon and electron–phonon interactions*

To obtain good agreement with experiment, it is necessary to include el–ph and electron–photon interactions in such calculations of the Raman intensity as a function of E_{laser}. In this connection, we here discuss the calculation of the electron–photon matrix elements (Sections 3.4 and 3.4.1) and of the el–ph matrix elements (Section 3.4.3), which are the matrix elements that appear in the numerator of the perturbation calculation of the Raman scattering amplitude (Section 3.6). Calculation of the Raman excitation profile (Section 3.6.3) in which the Raman intensity is observed as a function of E_{laser} is of great interest for obtaining the Raman intensity at resonance which is the quantity of greatest interest for experimental studies. Many experimental Raman studies that are found in the literature are actually not carried out under fully resonance conditions, but only within the resonance window, so care must be exercised in making proper comparisons between experiment and theory.

3.1.5. *Excitons*

In the case of carbon nanotubes, the exciton binding energy is much larger (up to 1 eV) [120–122,147,242] than that for Si (which is in the meV range). The exciton, which is formed from a photo-excited electron and the hole that is left behind, is especially important and dominates the observed optical processes in carbon nanotubes which are 1D systems where excitonic effects are exceedingly strong. Even at room temperature, the excitonically mixed electronic states are specified by a wavevector $\mathbf{k}$ so as to form a spatially localized state. In order to obtain excitonic states and their corresponding wavefunctions, the Bethe–Salpeter equation for π electrons is used here within the tight-binding method (Section 3.5). Using excitonic wavefunctions, we can calculate the relevant exciton–photon (Section 3.6) and exciton–phonon (Section 3.6.3) matrix elements. Two-photon absorption or time-dependent Raman spectroscopy have also been used to observe many specific exciton-related phenomena.

3.1.6. *Resonance window and the Kohn Anomaly*

Since the photo-excited electron (or hole) has a finite lifetime (less than 1 ps), the transition energy of an exciton has an energy uncertainty which is observed as an energy width in the measurement of the Raman excitation profile, which we also call the resonance window. A typical value for the experimentally reported resonance windows is 100 meV and the origin of the finite lifetime of the photo-excited carriers lies in the exciton–phonon scattering process, which depends on the metallicity, chiral angle and diameter of the SWNT. In the case of metallic nanotubes, phonons typically couple to an e–h pair excitation by the el–ph (or more precisely the exciton–phonon) interaction. Second-order perturbation theory for the phonon energy gives values for the energy shifts and spectral broadening that arise through the el–ph interaction, and we call these energy shifts and broadening effects the KA [127,194,197–199,243]. This topic is discussed in Section 3.6.5. The KA is observed experimentally in the G-band of graphene (Section 2.7.1) and in both the G-band and the RBM features for metallic nanotubes in gating or electro-chemical doping experiments Section 2.7.3 [196,203–205].

3.2. ***Tight-binding calculation for phonons***

The phonon energy dispersion can be calculated by using a force constant tensor which connects the relevant motion of nearest-neighbor atoms through these theoretical calculations. The equations of motion are given by

$$M_i \ddot{\mathbf{u}}_i = \sum_j K^{(ij)}(\mathbf{u}_j - \mathbf{u}_i), \quad (i = 1, \ldots, N), \tag{15}$$

where M_i and $\mathbf{u}_i$ are, respectively, the mass and the vibrational amplitude of the ith atom and $K^{(ij)}$ represents a 3×3 force constant tensor which connects ith and jth atoms. The summation on j is taken over the jth nearest neighbor atoms so as to reproduce the phonon energy dispersion relation (see Figure 30). The $K^{(ij)}$ terms are obtained by fitting to experimentally obtained phonon dispersion relations, such as are determined from neutron or X-ray inelastic scattering measurements [208,235,239]. The fitting procedure to the experimental phonon dispersion is possible even if the KA effect is included. However, the broadening of the phonon dispersion due to the finite lifetime

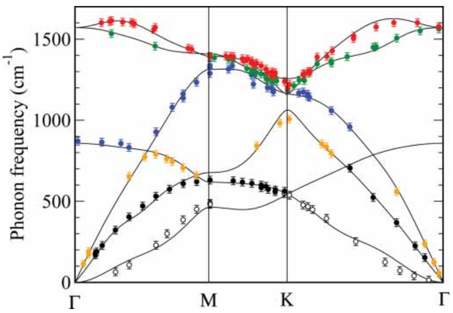

Figure 30. Phonon dispersion of graphene in the 2D BZ. The symbols are experimental data obtained by inelastic X-ray scattering [244] and the lines are fitted to the experimental phonon data using up to 14th nearest-neighbor interactions [245].

of phonon cannot be expressed by the present method and the self-energy for the phonon should then be calculated as discussed below [196,205,219,220,246].

Since the lattice is periodic, each displacement $\mathbf{u}_i$ in the unit cell can be expressed by a wave with a phonon wavevector $\mathbf{k}$ and frequency ω as follows:

$$\mathbf{u}_{\mathbf{k}}^{(i)} = \frac{1}{\sqrt{N_u}} \sum_{\mathbf{R_i}} \mathrm{e}^{i(\mathbf{k}\cdot\mathbf{R_i}-\omega t)} \mathbf{u}_i, \tag{16}$$

where the sum is taken over all N_u lattice vectors $\mathbf{R_i}$ in the crystal for the ith atom in the unit cell. The equation for $\mathbf{u}_{\mathbf{k}}^{(i)}$ $(i = 1, \ldots, N)$, where N is the number of atoms in the unit cell, is given by [32]

$$\left[\sum_j K^{(ij)} - M_i\omega^2(\mathbf{k})I\right]\mathbf{u}_{\mathbf{k}}^{(i)} - \sum_j K^{(ij)}\mathrm{e}^{i\mathbf{k}\cdot\Delta\mathbf{R_{ij}}}\mathbf{u}_{\mathbf{k}}^{(j)} = 0 \tag{17}$$

in which I is a 3×3 unit matrix and $\Delta\mathbf{R_{ij}} = \mathbf{R_i} - \mathbf{R_j}$ denotes the relative coordinate of the ith atom with respect to the jth atom. The simultaneous equations implied by Equation (17) with $3N$ unknown variables $\mathbf{u_k} \equiv {}^t(\mathbf{u}_{\mathbf{k}}^{(1)}, \mathbf{u}_{\mathbf{k}}^{(2)}, \ldots, \mathbf{u}_{\mathbf{k}}^{(N)})$, for a given $\mathbf{k}$ vector, can be solved by a diagonalization of the $3N \times 3N$ matrix in brackets, which we call the dynamical matrix. By diagonalizing the dynamical matrix for each $\mathbf{k}$, we get the phonon frequencies and corresponding amplitudes as a function of $\boldsymbol{k}$, $\omega(\boldsymbol{k})$ and $\mathbf{u_k}$, respectively, which are the eigenvalues and eigenfunctions of the dynamical matrix.

In Figure 30, the phonon dispersion relations of graphene are plotted in the 2D BZ. Lines are fitted for the calculated phonon energy dispersion to the experimental data for inelastic X-ray scattering (symbols) by a set of force constants that includes force constants up to 14th nearest neighbors [245]. This force constant set is obtained by minimizing the square of the difference between experiment and theory for each experimental data point. In order to get good convergence for the nonlinear fitting, we must start with a small number of nearest neighbors and we then increase the number of neighbors one by one. Further, in order to get the required zero value for the acoustic phonon modes at the Γ point, we should consider the relationships between the force constant set, known as the force constant set sum rule [217]. Degenerate in-plane optical phonon modes around 1600 cm^{-1} at the Γ point are known by symmetry requirements to correspond to the Raman-active phonon mode (G-band), while the out-of-plane optical (oTO) phonon mode around 860 cm^{-1} at the Γ point is an infrared-active phonon mode. The acoustic modes are discussed in [247].

The phonon modes near the K point and Γ point can be observed by defect-induced or two-phonon derived features in the Raman spectra. The phonon modes along the phonon dispersion relation can be observed by studying phonon modes arising from DR Raman processes (see Section 2.8.6) [210]. The LO phonon mode (the highest frequency mode) of graphene has a local minimum at the Γ point and the phonon energy increases with increasing k by a process which we call “over-bending”. The “over-bending” can be reproduced using force constants going beyond the fifth nearest neighbor. Both the in-plane optic phonon modes near the Γ point and the iTO phonon mode near the K point show phonon softening phenomena for graphene and metallic SWNTs and the resulting phonon frequency down-shifts are known as the KA effect [127,194,196–199,205,219,220,243,246] (see Section 3.6.5). When we calculate phonon dispersion by first principles [248–250], the effect of the Kohn anomalies should be taken into account when calculating a force constant set, while in the simple tight-binding method, we just obtain a force constant set either by fitting to the experimental results [208,244,251,252] or by first-principles calculation in which the Kohn anomalies are taken into account. When we obtain a force constant set by the atomic potential as a function of the C–C bond distance, such as by the extended tight-binding method [253,254], we should consider the additional effect of the KA in the calculation.

Interlayer force constants of multi-layer graphene are much weaker than the intralayer force constant set. Each phonon mode of a graphene sheet is split into symmetric and anti-symmetric vibrational modes with respect to the inversion or mirror symmetry of multi-layers, depending on whether the multilayer graphene consists of an even or odd number of graphene layers, respectively. It is important that some phonon modes (oTO, oTA, LO) become Raman active (or inactive) by the interlayer interaction [4].

3.3. *Simple tight-binding calculation for the electronic structure*

Tight-binding calculations of the electronic energy bands for sp^2 carbons are useful for understanding the physics of sp^2 carbons and for saving computational time. The tight-binding wavefunction $\Psi_j(\vec{k})$, where j denotes the energy band index, is given by a linear combination of a small number of tight-binding Bloch wave functions $\Phi_{j'}$

$$\Psi_j(\vec{k},\vec{r}) = \sum_{j'=1}^{N} C_{jj'}(\vec{k})\Phi_{j'}(\vec{k},\vec{r}) \quad (j = 1,\dots,N), \tag{18}$$

where $C_{jj'}(\vec{k})$ are coefficients to be determined and N the number of atomic orbitals in the unit cell. When we consider π orbitals for n-layer graphene, then $N = 2n$. Here Φ_j denotes the Bloch function for an atomic orbital φ_j which is given by

$$\Phi_j(\vec{k},\vec{r}) = \frac{1}{\sqrt{N_u}} \sum_{\vec{R}}^{N_u} \mathrm{e}^{i\vec{k}\cdot\vec{R}} \varphi_j(\vec{r}-\vec{R}) \quad (j = 1,\dots,N), \tag{19}$$

where the summation takes place over N_u lattice vectors $\vec{R}$ in the crystals. When we put Equation (18) into the Schrödinger equation $\mathcal{H}\Psi_j = E\Psi_j$ for a Hamiltonian $\mathcal{H}$, we get

$$\sum_{j'=1}^{N} \mathcal{H}_{jj'}(\vec{k})C_{ij'} = E_{\mathrm{i}}(\vec{k}) \sum_{j'=1}^{N} \mathcal{S}_{jj'}(\vec{k})C_{ij'} \quad (i = 1,\dots,N). \tag{20}$$

Here $\mathcal{H}_{jj'}(\vec{k})$ and $\mathcal{S}_{jj'}(\vec{k})$ are the Hamiltonian, and the overlap matrices are defined by

$$\mathcal{H}_{jj'}(\vec{k}) = \langle \Phi_j|\mathcal{H}|\Phi_{j'}\rangle, \quad \mathcal{S}_{jj'}(\vec{k}) = \langle \Phi_j|\Phi_{j'}\rangle \quad (j,j' = 1,\ldots,N). \tag{21}$$

By defining a column vector $\mathbf{C}_i$ as

$$\mathbf{C}_i = \begin{pmatrix} C_{i1} \\ \vdots \\ C_{iN} \end{pmatrix}, \tag{22}$$

then Equation (20) is expressed by the eigenvalue equation

$$\mathcal{H}\mathbf{C}_i = E_{\mathrm{i}}(\vec{k})\mathcal{S}\mathbf{C}_i. \tag{23}$$

By diagonalization of a given $\mathcal{H}$ and $\mathcal{S}$ for each $\vec{k}$ vector, we get the energy eigenvalues $E_{\mathrm{i}}(\vec{k})$ and eigenfunctions $\mathbf{C}_i(\vec{k})$.

The ij matrix element of $\mathcal{H}$ is given by

$$\begin{aligned} \mathcal{H}_{ij}(\vec{k}) &= \frac{1}{N_u}\sum_{R,R'} \mathrm{e}^{ik(R-R')}\langle\varphi_i(r-R')|\mathcal{H}|\varphi_j(r-R)\rangle \\ &= \sum_{\Delta R} \mathrm{e}^{ik(\Delta R)}\langle\varphi_i(r-\Delta R)|\mathcal{H}|\varphi_j(r)\rangle, \end{aligned} \tag{24}$$

where $\Delta R \equiv R - R'$ and in the second of line of Equation (24), we use the fact that the tight-binding parameter $\langle\varphi_i(r-R')|\mathcal{H}|\varphi_j(r-R)\rangle$ only depends on ΔR. Similarly, the matrix elements of $\mathcal{S}$ are given by

$$\mathcal{S}_{ij}(\vec{k}) = \sum_{\Delta R} \mathrm{e}^{ik(\Delta R)}\langle\varphi_i(r-\Delta R)|\varphi_j(r)\rangle. \tag{25}$$

The tight-binding parameters $\langle\varphi_i(r-\Delta R)|\mathcal{H}|\varphi_j(r)\rangle$ and $\langle\varphi_i(r-\Delta R)|\varphi_j(r)\rangle$ are obtained by: (1) integrating the matrix elements using the atomic orbitals $\varphi_j(r)$ [247] or (2) fitting them so as to reproduce experimentally obtained energy dispersion measurements. Values for a typical fitted parameter set (TBP) are listed in Table 1.

As seen in Table 1, tight-binding parameters are listed for up to the third nearest neighbor (3NN) within a layer (upper half) and for interlayer interactions between graphene layers (lower half) [255]. In Figure 31, we show a definition of the tight-binding parameters listed in Table 1 for the Hamiltonian for pairs of carbon atoms separated by their corresponding distances ΔR [255]. The notation used for the parameters γ_i follows that of Slonczewski and Weiss [257], while γ_0^j and s_j $(j = 1, 2, 3)$ denote the in-plane parameters with the jth nearest neighbors up to the 3rd nearest neighbor (3NN). As far as we consider transport properties near the K point of the first BZ, the in-plane nearest-neighbor parameter γ_0^1 is sufficient. However, when we consider optical transition phenomena around the K point, it is necessary to include the parameters γ_0^2 and γ_0^3 which are indicated explicitly in Figure 31 [256]. The parameters γ_1, γ_3 and γ_4 denote interactions between carbon atoms in the nearest-neighbor layers, while the parameters γ_2 and γ_5 couple carbon atoms in next nearest-neighbor layers. The parameters γ_3 and γ_4 introduce a **k**-dependent interlayer interaction and γ_2 sensitively determines a small energy dispersion along the KH direction in the 3D BZ for energy bands near the Fermi energy of graphite (see [5, Fig. 1f]) which gives rise to the semi-metallic nature of 3D graphite.

The overlap tight-binding parameters, s_0, s_1 and s_2, are essential for describing the asymmetry between the valence and conduction energy bands relative to the Fermi energy. The energy band

Table 1. Third nearest-neighbor tight-binding (3NN TB) parameters for few-layer graphene and graphite.

TBP	3NN TB-**GW**[a]	3NN TB-LDA[a]	EXP[b]	3NN TB-LDA[c]	ΔR, pair[d]
γ_0^1	−3.4416	−3.0121	−5.13	−2.79	$a/\sqrt{3}$, AB
γ_0^2	−0.7544	−0.6346	1.70	−0.68	a, AA and BB
γ_0^3	−0.4246	−0.3628	−0.418	−0.30	$2a/\sqrt{3}$, AB
s_0	0.2671	0.2499	−0.148	0.30	$a/\sqrt{3}$, AB
s_1	0.0494	0.0390	−0.0948	0.046	a, AA and BB
s_2	0.0345	0.0322	0.0743	0.039	$2a/\sqrt{3}$, AB
γ_1	0.3513	0.3077	–	–	c, AA
γ_2	−0.0105	−0.0077	–	–	$2c$, BB
γ_3	0.2973	0.2583	–	–	$(a/\sqrt{3},c)$, BB
γ_4	0.1954	0.1735	–	–	$(a/\sqrt{3},c)$, AA
γ_5	0.0187	0.0147	–	–	$2c$, AA
E_0^{e}	−2.2624	−1.9037	–	−2.03	
Δ^{f}	0.0540[g]	0.0214	–	–	

[a] Fits to LDA and *GW* calculations [255].
[b] Fit to ARPES experiments by Rotenberg *et al.* [124].
[c] Fit to LDA calculations by Reich *et al.* [256].
[d] In-plane and out-of-plane distances between a pair of A and B atoms.
[e] The energy position of π orbitals relative to the vacuum level.
[f] Difference of the diagonal term between A and B atoms for multi-layer graphene.
[g] The impurity doping level is adjusted in order to reproduce the experimental value of Δ in graphite.

All values are in eV except the dimensionless overlap parameters of s_0-s_2. The parameters of fits to LDA and *GW* calculations are shown. The 3NN Hamiltonian is valid over the whole 2-D (3-D) BZ of graphite (graphene layers) [255]. Mopac93 and Gaussian 9 software packages were used for implementing Gaussian and other software applications.

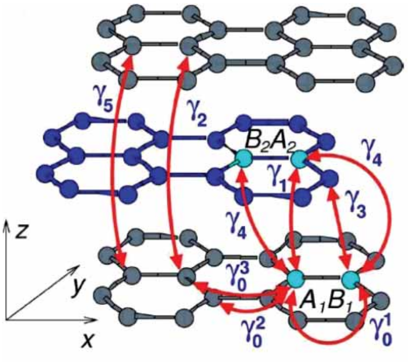

Figure 31. Identification of the various Slonczewski–Weiss parameters for the tight-binding parameters for a pair of carbon atoms separated by a distance ΔR. Adapted figure with permission from A. Grüneis *et al.*, Physical Review B 78, p. 205425, 2008 [255]. Copyright © (2008) by the American Physical Society.

width of the conduction band is larger than that of the valence band when using this set of tight-binding parameters [32], thereby inducing asymmetry between the electrons and holes in few layer graphene. Further, depending on whether the number of graphene layers is odd (even), the linear (quadratic) k energy dispersion behavior appears near the K point. Koshino and Ando [258] have explained analytically the reason for the odd-even dependence of the electronic structure of few layer graphene on the number of graphene layers by the tight-binding method.

3.3.1. *Extended tight-binding calculation for the graphene electronic structure*

The simple tight-binding parameters obtained in Section 3.3 are only for π orbitals in graphene. When we consider SWNTs, the curvature of the cylindrical tube surface should be considered. The curvature effect mixes π orbitals with σ orbitals ($2p_x$, $2p_y$ and 2s). Furthermore, when we consider the geometrical optimization of the lattice, we need to calculate tight-binding parameters as a function of the actual C–C bonds.

The extended tight-binding (ETB) calculation is a tight-binding calculation for π, σ and 2s orbitals, in which the tight-binding parameters for a pair of orbitals are given as a function of the C–C bond lengths and bond angles. The basic treatment of the mixing between π and σ orbitals uses a formalism known as the Slater–Koster method in which p orbitals can be projected on to a chemical bond [259]. Values for the ETB parameters as a function of the C–C bond length are given by first-principles calculations for several sp^2 molecules or solids. For carbon systems, the tight-binding parameters as a function of the C–C bond length have been calculated by Porezag [253], and the optimized structure of SWNTs using ETB parameters reproduced well the transition energy separation E_{ii} especially for SWNTs with diameters smaller than 1 nm [254].

In quantum chemistry calculations, great effort has been given to ETB-like calculations for reproducing the energy levels for many different molecules, which are known as semi-empirical methods. MNDO, MINDO, AM3 and PM5 are names of the parameter sets for popular semi-empirical methods, which are used in many chemistry molecular level calculations, such as MOPAC [260] and Gaussian [261], etc. An advantage of the ETB or the semi-empirical methods is that the calculation is fast and small in size. This calculational approach is suitable for the calculation of SWNTs since a SWNT has a large number of carbon atoms in the unit cell.

3.4. ***Calculations of matrix elements***

Using the electronic and phonon eigenfunctions, we can calculate the matrix elements for the electron–photon and el–ph interactions.

3.4.1. *The electron–photon matrix element*

Using the simple tight-binding wavefunction, the electron–photon matrix element is calculated within the dipole approximation. The perturbation Hamiltonian of the optical dipole transition is given by

$$H_{\mathrm{opt}} = \frac{ie\hbar}{m}\mathbf{A}(t)\cdot\nabla, \tag{26}$$

where $\mathbf{A}$ is the vector potential. When we adopt the Coulomb gauge $\nabla\cdot\mathbf{A}(t) = 0$, the electric field of the light is given by $\mathbf{E} = i\omega\mathbf{A}$. Hereafter, we consider only a linear polarization of the light, and thus the vector potential $\mathbf{A}$ is given by

$$\mathbf{A} = \frac{-\mathrm{i}}{\omega}\sqrt{\frac{I}{c\epsilon_0}}\exp(\pm\mathrm{i}\omega t)\mathbf{P}, \tag{27}$$

where $\mathbf{P}$ is the unit vector (polarization vector) which specifies the direction of $\mathbf{E}$, I the intensity of the light in W/m^2 and ϵ_0 the dielectric constant for the vacuum in SI units. The "±" sign corresponds to the emission ("+") or absorption ("−") of a photon with frequency ω. Here, we can assume that the wavevector $\boldsymbol{k}$ of an electron does not change during the transition (vertical transition). Then the matrix element for optical transitions from an initial state $\Psi^i(\mathbf{k})$ to a final state $\Psi^f(\mathbf{k})$ at $\mathbf{k}$ is defined by

$$\mathbf{M}^{f\iota}_{\mathrm{opt}}(\mathbf{k}) = \langle \Psi^f(\mathbf{k}) | H_{\mathrm{opt}} | \Psi^\iota(\mathbf{k}) \rangle. \tag{28}$$

The electron–photon matrix element between initial and final states in Equation (28) is calculated by

$$\mathbf{M}^{f\iota}_{\mathrm{opt}}(\mathbf{k}) = \frac{e\hbar}{m\omega_\rho}\sqrt{\frac{I_\rho}{c\epsilon_0}}\,\mathrm{e}^{i(\omega_{\mathrm{F}}-\omega_\iota\pm\omega)t}\mathbf{D}^{f\iota}(\mathbf{k})\cdot\mathbf{P} \tag{29}$$

where the weak spatial dependence of the vector potential A is neglected and $\mathbf{D}^{f\iota}(\mathbf{k})$ is the dipole vector defined by the matrix element

$$\mathbf{D}^{f\iota}(\mathbf{k}) = \langle \Psi^f(\mathbf{k}) | \nabla | \Psi^\iota(\mathbf{k}) \rangle. \tag{30}$$

For a given polarization, $\mathbf{P}$, the optical absorption (or stimulated emission) becomes large (absent) when $\mathbf{D}$ is parallel (perpendicular) to $\mathbf{P}$.

3.4.2. *Electric dipole vector for graphene*

When we expand Ψ in Equation (30) into atomic orbitals $\varphi_j(\vec{r}-\vec{R})$ (Equation (19)), the dipole vector $\mathbf{D}$ can be expressed by the atomic dipole vector $\langle \varphi_j(\vec{r}-\vec{R}')|\nabla|\varphi_j(\vec{r}-\vec{R})\rangle$. The optical dipole transition of an electron from a π (2p$_z$) band to an unoccupied π^* band within an atom ($\vec{R}' = \vec{R}$) is forbidden in the case of graphene, which is understood by the mirror symmetry occurring at $z = 0$. However, the optical transition between a π and a π^* energy band is possible when the optical transition between nearest-neighbor interaction is allowed, as shown below.

Here, we consider the electric dipole vector for graphene [262]. The wavefunction in Equation (18) with $N = 2$ is given by $\Psi(\mathbf{k}) = C_{\mathrm{A}}\Phi_{\mathrm{A}}(\mathbf{k},\mathbf{r}) + C_B\Phi_B(\mathbf{k},\mathbf{r})$, in which Φ is the Bloch wavefunction for $2p_z$ atomic orbitals for the A and B sites of graphene. If we neglect the next nearest-neighbor interaction between the A and A atoms (or the B and B atoms), the electric dipole vector $\mathbf{D}^{f\iota}(\mathbf{k}_{\mathrm{F}},\mathbf{k}_\iota)$ for graphene is given by,

$$\begin{aligned}\mathbf{D}^{f\iota}(\mathbf{k}_{\mathrm{F}},\mathbf{k}_\iota) &= C^{f*}_B(\mathbf{k}_{\mathrm{F}})C^\iota_{\mathrm{A}}(\mathbf{k}_\iota)\langle \Phi_B(\mathbf{k}_{\mathrm{F}},\mathbf{r})|\nabla|\Phi_{\mathrm{A}}(\mathbf{k}_\iota,\mathbf{r})\rangle \\ &\quad + C^{f*}_{\mathrm{A}}(\mathbf{k}_{\mathrm{F}})C^\iota_B(\mathbf{k}_\iota)\langle \Phi_{\mathrm{A}}(\mathbf{k}_{\mathrm{F}},\mathbf{r})|\nabla|\Phi_B(\mathbf{k}_\iota,\mathbf{r})\rangle.\end{aligned} \tag{31}$$

Since both the 2p$_z$ orbital and the $\partial/\partial z$ component of ∇ have odd symmetry with respect to the z mirror plane, the z component of $\mathbf{D}$ becomes zero. Thus, we conclude that the dipole vector lies in the xy plane.

When we expand Ψ into atomic orbitals, the leading term of $\langle \Phi_{\mathrm{A}}(\mathbf{k}_{\mathrm{F}},\mathbf{r})|\nabla|\Phi_B(\mathbf{k}_\iota,\mathbf{r})\rangle$ is the atomic matrix element m_{opt} between nearest neighbor atoms given by

$$m_{\mathrm{opt}} = \left\langle \phi(\mathbf{r}-\mathbf{R}_{\mathrm{nn}}) \left| \frac{\partial}{\partial x} \right| \phi(\mathbf{r}) \right\rangle, \tag{32}$$

where $\mathbf{R}_{\mathrm{nn}}$ is the lattice vector between nearest-neighbor C atoms along the x-axis.

When we use a linear approximation for the coefficients C_A and C_B for a $\mathbf{k}$ point around the corner point of the 2D BZ $\mathbf{K} = (0, -4\pi/(3a))$ for the valence (v) and conduction (c) bands, we

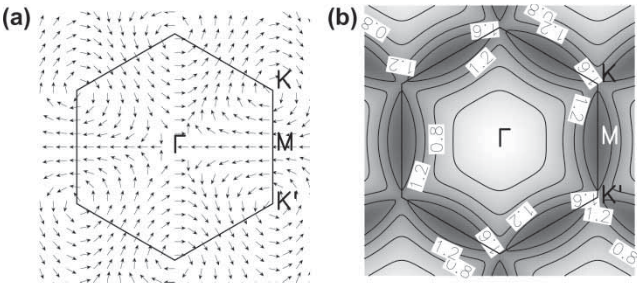

Figure 32. (a) The normalized dipole vector $\mathbf{D}^{\mathrm{cv}}(\mathbf{k})$ is plotted as a function of $\mathbf{k}$ over the 2D BZ. (b) The oscillator strength in units of the atomic matrix element m_{opt} is plotted as a function of $\mathbf{k}$ over the 2D BZ. The separation between two adjacent contour lines is 0.4 m_{opt}. The darker areas have a larger value for the oscillator strength. Reprinted figure with permission from A. Grüneis *et al.*, Physical Review B 67, pp. 165402–165407, 2003 [262]. Copyright © (2003) by the American Physical Society.

write [32]

$$\begin{aligned} C^{v}_{\mathrm{A}}(\mathbf{K}+\mathbf{k}) &= \frac{1}{\sqrt{2}}, \quad C^{v}_{B}(\mathbf{K}+\mathbf{k}) = \frac{k_y - \mathrm{i}k_x}{\sqrt{2}k}. \\ C^{c}_{\mathrm{A}}(\mathbf{K}+\mathbf{k}) &= \frac{1}{\sqrt{2}}, \quad C^{c}_{B}(\mathbf{K}+\mathbf{k}) = \frac{-k_y + \mathrm{i}k_x}{\sqrt{2}k}, \end{aligned} \tag{33}$$

The electric dipole vector coupling the valence and conduction bands is then given by

$$\mathbf{D}^{\mathrm{cv}}(\mathbf{K}+\mathbf{k}) \equiv \langle \Psi^{c}(\mathbf{K}+\mathbf{k}) | \vec{\nabla} | \Psi^{v}(\mathbf{K}+\mathbf{k}) \rangle = \frac{3m_{\mathrm{opt}}}{2k}(k_y, -k_x, 0). \tag{34}$$

In Figure 32(a) we plot the normalized directions of the normalized dipole vector $\mathbf{D}^{\mathrm{cv}}(\mathbf{k})$ as arrows over the 2D BZ of graphene [262]. Around the K points, the arrows show a vortex behavior. Note also that the rotational directions of $\mathbf{D}^{\mathrm{cv}}(\mathbf{k})$ around the K and K' points are opposite to each other in Figure 32(a). In Figure 32(b) we plot the values of the magnitude of the oscillator strength $O(\mathbf{k})$ in units of m_{opt} on a contour plot. Here $O^{\mathrm{cv}}(\mathbf{k})$ is defined by

$$O^{\mathrm{cv}}(\mathbf{k}) = \sqrt{\mathbf{D}^{cv*}(\mathbf{k}) \cdot \mathbf{D}^{\mathrm{cv}}(\mathbf{k})}. \tag{35}$$

As shown in Figure 32(b), the oscillator strength $O^{\mathrm{cv}}(\mathbf{k})$ has a maximum at the M points and a minimum at the Γ point in the 2D BZ. The $\mathbf{k}$ dependent $O^{\mathrm{cv}}(\mathbf{k})$ will be relevant to the calculation for the type-dependent photoluminescence (PL) intensity of a single wall S-SWNT [263] in which the PL of type I $(\mathrm{mod}(2n+m,3)=1)$ is stronger than for type II $(\mathrm{mod}(2n+m,3)=2)$ S-SWNTs, though we need to consider the electric dipole vector for each carbon nanotube individually in terms of its diameter and chiral angle [262,264,265].

The optical absorption intensity is given by the inner product $\mathbf{D}^{\mathrm{cv}}(\mathbf{k}) \cdot \mathbf{P}$ up to linear terms in k_x and k_y for a given polarization vector $\mathbf{P} = (p_x, p_y, p_z)$

$$\mathbf{P} \cdot \mathbf{D}^{\mathrm{cv}}(\mathbf{K}+\mathbf{k}) = \pm\frac{3m_{\mathrm{opt}}}{2k}(p_y k_x - p_x k_y). \tag{36}$$

Equation (36) shows that the line $p_y k_x - p_x k_y = 0$ in the 2D BZ denotes the conditions for the occurrence of a node in the optical absorption for a given polarization vector $\mathbf{P} = (p_x, p_y)$. In the case of graphene, however, the optical transition events take place along equi-energy contours around the K points, and we cannot see the nodes. This phenomena might be observed in graphene nanoribbons in which a 1D k value is specially selected. The polarization dependence of the optical absorption relative to the edge of graphene nanoribbon is now an interesting problem. In the case of a normal semiconductor, since the dipole vector is not a linear function of k, we cannot get a node in such cases.

3.4.3. *Calculation of the electron–phonon interaction*

The el–ph interaction which is the focus of this section is expressed by a modification to the tight-binding parameters that are pertinent to describing the lattice vibrations. In most theoretical works on the el–ph interaction, modification to the electron transfer energy as a function of the C–C bond length is considered for only the nearest neighbor C–C bonds as a parameter [219,220,266]. Here we calculated the el–ph interaction not only for long distance C–C bonds, but also for the so-called on-site el–ph interaction in which the site energy is modified by the vibration [267,268]. Their values are obtained by using the wavefunction and atomic potential as a function of the C–C distance [253].

Here, we rewrite the wavefunctions appearing in Equations (18) and (19) using a different notation, which is suitable for calculating the el–ph matrix elements [268]. We then write the Bloch functions

$$\Psi_{a,\mathbf{k}}(\mathbf{r}) = \frac{1}{\sqrt{N_u}} \sum_{s,o} C_{s,o}(a,\mathbf{k}) \sum_{\mathbf{R}_t} \mathrm{e}^{i\mathbf{k}\cdot\mathbf{R}_t} \phi_{t,o}(\mathbf{r}-\mathbf{R}_t), \tag{37}$$

where $s = A$ and B is an index denoting the two carbon atoms in the unit cell, and $\mathbf{R}_t$ denotes the equilibrium atom positions relative to the origin. $\phi_{t,o}$ denotes the atomic wave functions for the orbitals $o = 2\mathrm{s}, 2\mathrm{p}_x, 2\mathrm{p}_y$ and $2\mathrm{p}_z$ at $\mathbf{R}_t$, which are real functions (with no imaginary components).

The potential energy of the lattice V can be expressed by the atomic potentials $v(\mathbf{r}-\mathbf{R}_t)$ at $\mathbf{R}_t$,

$$V = \sum_{\mathbf{R}_t} v(\mathbf{r}-\mathbf{R}_t), \tag{38}$$

where v in Equation (38) is given by the first-principles calculation for the Kohn–Sham potential of a neutral pseudo-atom [253]. The matrix element for the potential energy between the two different states $\Psi_i = \Psi_{a,\mathbf{k}}$ and $\Psi_f = \Psi_{a',\mathbf{k}'}$ is then written as

$$\begin{aligned} \langle \Psi_{a',\mathbf{k}'}(\mathbf{r})|V|\Psi_{a,\mathbf{k}}(\mathbf{r})\rangle = {} & \frac{1}{N_u} \sum_{s',o'} \sum_{s,o} C^*_{s',o'}(a',\mathbf{k}') C_{s,o}(a,\mathbf{k}) \\ & \times \sum_{u'} \sum_{u} \mathrm{e}^{i(-\mathbf{k}'\cdot\mathbf{R}_{u',s'}+\mathbf{k}\cdot\mathbf{R}_{u,s})} m(t',o',t,o), \end{aligned} \tag{39}$$

with the matrix element m for the atomic potential given by

$$m = \int \phi_{s',o'}(\mathbf{r}-\mathbf{R}_{t'}) \left\{ \sum_{\mathbf{R}_{t''}} v(\mathbf{r}-\mathbf{R}_{t''}) \right\} \phi_{s,o}(\mathbf{r}-\mathbf{R}_t)\,\mathrm{d}\mathbf{r}. \tag{40}$$

The atomic matrix element m thus comes from an integration over three centers of atoms, $\mathbf{R}_t$, $\mathbf{R}_{t'}$ and $\mathbf{R}_{t''}$. We neglect m for the cases for which the three centers t, t' and t'' are different from one another. When we consider only two center integrals, m consists, respectively, of off-site and on-site matrix elements m_α and m_λ as follows:

$$\begin{aligned} m_\alpha &= \int \phi_{s',o'}(\mathbf{r}-\mathbf{R}_{t'})\{v(\mathbf{r}-\mathbf{R}_{t'})+v(\mathbf{r}-\mathbf{R}_t)\}\phi_{s,o}(\mathbf{r}-\mathbf{R}_t)\,\mathrm{d}\mathbf{r}, \\ m_\lambda &= \int \phi_{s',o'}(\mathbf{r}-\mathbf{R}_t)\left\{\sum_{\mathbf{R}_{t'}\neq\mathbf{R}_t} v(\mathbf{r}-\mathbf{R}_{t'})\right\}\phi_{s',o}(\mathbf{r}-\mathbf{R}_t)\,\mathrm{d}\mathbf{r}. \end{aligned} \tag{41}$$

The potential $v(\mathbf{r}-\mathbf{R}_i)$ is vibrating within an adiabatic approximation with a phonon amplitude $\mathbf{S}(\mathbf{R}_t)$. Then the potential modification δV due to a lattice vibration is given by

$$\begin{aligned} \delta V &= \sum_{\mathbf{R}_t} v[\mathbf{r}-\mathbf{R}_t-\mathbf{S}(\mathbf{R}_t)] - v(\mathbf{r}-\mathbf{R}_t) \\ &\approx -\sum_{\mathbf{R}_t} \nabla v(\mathbf{r}-\mathbf{R}_t)\cdot\mathbf{S}(\mathbf{R}_t). \end{aligned} \tag{42}$$

Since the potential modification δV breaks the periodicity of the lattice, the wavevector for an electron is no longer a good quantum number and thus the scattering of an electron by the el–ph interaction occurs. If we consider δV as a perturbation, then the el–ph matrix element is defined on the basis of perturbation theory: as [139,267–270]

$$\begin{aligned} M_{a,\mathbf{k}\to a',\mathbf{k}'} &\equiv \langle \Psi_{a',\mathbf{k}'}(\mathbf{r})|\delta V|\Psi_{a,\mathbf{k}}(\mathbf{r})\rangle \\ &= -\frac{1}{N_u}\sum_{s',o'}\sum_{s,o} C^*_{s',o'}(a',\mathbf{k}')C_{s,o}(a,\mathbf{k})\sum_{u',u} \mathrm{e}^{i(-\mathbf{k}'\cdot\mathbf{R}_{u',s'}+\mathbf{k}\cdot\mathbf{R}_{u,s})}\delta m(t',o',t,o), \end{aligned} \tag{43}$$

where $\delta m(t',o',t,o)$ is the atomic deformation potential which consists of the off-site and on-site deformation potentials δm_α and δm_λ given by

$$\begin{aligned} \delta m_\alpha &= \int \phi_{s',o'}(\mathbf{r}-\mathbf{R}_{t'})\{\nabla v(\mathbf{r}-\mathbf{R}_{t'})\cdot\mathbf{S}(\mathbf{R}_{t'})+\nabla v(\mathbf{r}-\mathbf{R}_t)\cdot\mathbf{S}(\mathbf{R}_t)\}\times\phi_{s,o}(\mathbf{r}-\mathbf{R}_t)\,\mathrm{d}\mathbf{r}, \\ \delta m_\lambda &= \delta_{\mathbf{R}_t,\mathbf{R}_{t'}}\int \phi_{s',o'}(\mathbf{r}-\mathbf{R}_{t'})\left\{\sum_{\mathbf{R}_{t''}\neq\mathbf{R}_{t'}} \nabla v(\mathbf{r}-\mathbf{R}_{t''})\cdot\mathbf{S}(\mathbf{R}_{t''})\right\}\phi_{s',o}(\mathbf{r}-\mathbf{R}_{t'})\,\mathrm{d}\mathbf{r}. \end{aligned} \tag{44}$$

It is noted that both terms δm_α and δm_λ are of the same order of magnitude and that they work in a different way for each phonon mode [271].

The atomic deformation potential for any orbitals and for any vibration can be expressed by a small number of terms which are defined by the bonding or force constants between atoms along or perpendicular to the two atoms by using the Slater–Koster scheme [32,253]. The atomic el–ph matrix elements $\langle\phi|\nabla v|\phi\rangle$ are thus defined for four fundamental hopping and overlap integrals denoted by (ss), $(s\sigma)$, $(\sigma\sigma)$ and $(\pi\pi)$, which are defined as a function of the C–C distance [253, 268] as follows:

$$\begin{aligned} \vec{\alpha}_p(\tau) &= \int \phi_\mu(\mathbf{r})\nabla v(\mathbf{r})\phi_\nu(\mathbf{r}-\boldsymbol{\tau})\,\mathrm{d}\mathbf{r} = \alpha_p(\tau)\hat{I}(\alpha_p), \\ \vec{\lambda}_p(\tau) &= \int \phi_\mu(\mathbf{r})\nabla v(\mathbf{r}-\boldsymbol{\tau})\phi_\nu(\mathbf{r})\,\mathrm{d}\mathbf{r} = \lambda_p(\tau)\hat{I}(\lambda_p), \end{aligned} \tag{45}$$

which are, respectively, denoted by $\vec{\alpha}_p(\tau)$ and $\vec{\lambda}_p(\tau)$ for the off-site and on-site deformation potentials. Here $\hat{I}(\alpha_p)$ and $\hat{I}(\lambda_p)$ are unit vectors describing the direction of the off-site and on-site

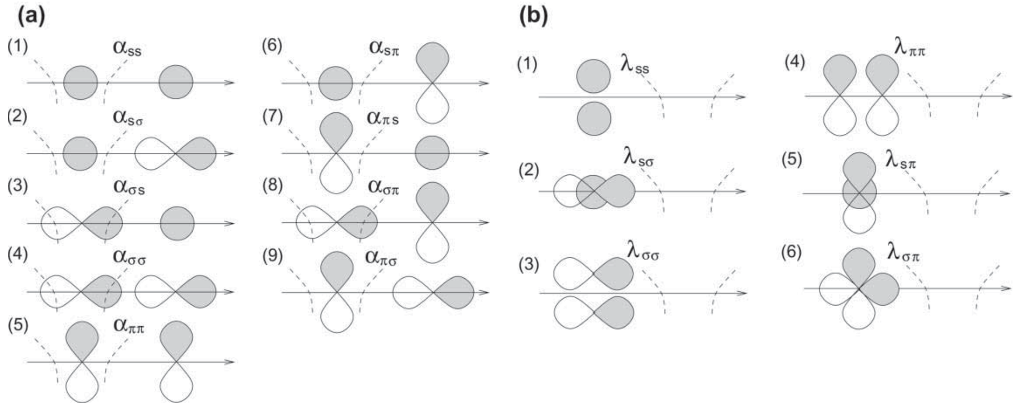

Figure 33. (a) The nine non-zero off-site deformation potential vectors $\vec{\alpha}_p$. The dashed curves represent the atomic potentials. (b) The six non-zero on-site deformation potential vectors $\vec{\lambda}_p$. The dashed curves represent the atomic potentials. For $\lambda_{ss}, \lambda_{\sigma\sigma}$ and $\lambda_{\pi\pi}$, the two same orbitals are illustrated by shifting them with respect to each other. Reprinted figure with permission from J. Jiang *et al.*, Physical Review B 72, pp. 235408–235411, 2005 [268]. Copyright © (2005) by the American Physical Society.

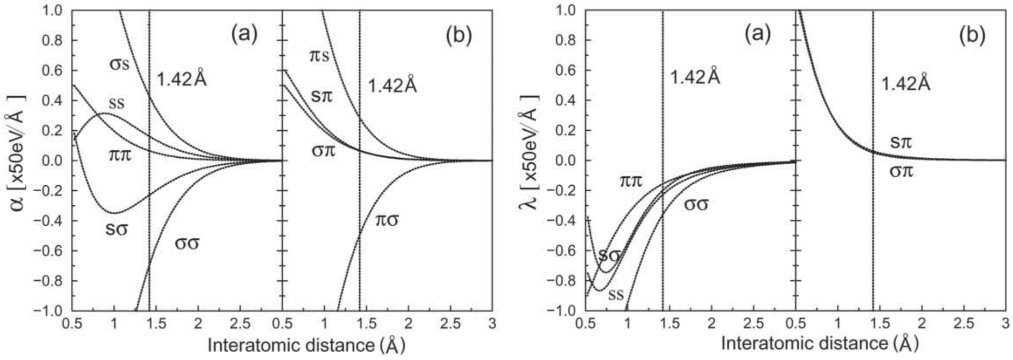

Figure 34. (a) The off-site deformation potential $\vec{\alpha}_p$ and (b) the on-site deformation potential $\vec{\lambda}_p$ as a function of inter-atomic distance. The vertical line corresponds to 1.42 Å which is the C–C distance in graphite Reprinted figure with permission from J. Jiang *et al.*, Physical Review B 72, pp. 235408–235411, 2005 [268]. Copyright © (2005) by the American Physical Society.

deformation potential vectors $\vec{\alpha}_p$ and $\vec{\lambda}_p$, respectively [271], and $p = \mu\nu$ as given in Equation (45). The 2p orbital ϕ_μ (ϕ_ν) is along or perpendicular to the bond connecting the two carbon atoms and τ is the distance between the two atoms.[17] In Figure 33, we show the non-zero matrix elements for the (a) off-site $\vec{\alpha}_p$ and (b) on-site $\vec{\lambda}_p$ atomic deformation potentials for 2s, σ and π atomic orbitals.

In Figure 34, the calculated values of $\vec{\alpha}_p$ and $\vec{\lambda}_p$ are plotted as a function of inter-atomic distance between two carbon atoms [268]. At $r = 1.42$ Å, which is the bond length between a carbon atom and one of its nearest neighbors, we have $\alpha_{\pi\pi} \approx 3.2$ eV/Å, and $|\lambda_{\pi\pi}| \approx 7.8$ eV/Å, and $|\alpha_{\pi\sigma}| \approx 24.9$ eV/Å. In order to calculate the el–ph matrix element of Equation (43) for each phonon mode, the amplitude of the atomic vibration $\mathbf{S}(\mathbf{R}_t)$ for the phonon mode $(\nu, \mathbf{q})$ is calculated by

$$\mathbf{S}(\mathbf{R}_t) = A_\nu(\mathbf{q})\sqrt{\bar{n}_\nu(\mathbf{q})}\mathbf{e}^\nu(\mathbf{R}_t)\mathrm{e}^{\pm i\omega_\nu(\mathbf{q})t}. \tag{46}$$

Here ± is for phonon emission (+) and absorption (−), respectively, and A, $\bar{n}$, $\mathbf{e}$ and ω are the zero-point phonon amplitude, number, eigenvector, and frequency, respectively. At equilibrium, the phonon number in Equation (46) is determined by the Bose–Einstein distribution function $n_\nu(\mathbf{q})$ for phonon ν:

$$n_\nu(\mathbf{q}) = \frac{1}{\mathrm{e}^{\hbar\omega/k_B T} - 1}. \tag{47}$$

Here, $T = 300\,\mathrm{K}$ is the lattice temperature at room temperature and k_B is the Boltzmann constant. For phonon emission, the phonon number is $\bar{n} = n + 1$, while for phonon absorption, $\bar{n} = n$. The amplitude of the zero-point phonon vibration is

$$A_\nu(\mathbf{q}) = \sqrt{\frac{\hbar}{N_u M_\mathrm{C} \omega_\nu(\mathbf{q})}}, \tag{48}$$

where M_C is the mass of a carbon atom and the phonon eigenvector $\mathbf{e}^\nu(\mathbf{R}_t)$ is given by diagonalizing the dynamical matrix Eq. $(17)^{18}$.

3.5. *Calculation of excitonic states*

In order to calculate the excitonic states, we first introduce in section 3.5.1 the Bethe–Salpeter equation Equation (49) which makes a localized wavefunction in real space. Using the exciton wavefunction, we show how to obtain the exciton–photon matrix element in Section 3.5.2 and the exciton–phonon matrix element in Section 3.5.3 within the tight-binding method.

3.5.1. *The Bethe–Salpeter equation for exciton states*

The exciton is a photo-excited electron and hole pair that is bonded by an attractive Coulomb interaction. In a SWNT, because of its 1D properties, the e–h binding energy becomes as large as 1 eV, so that exciton effects can be observed even at room temperature. Thus excitons are essential for explaining optical processes in SWNTs, such as optical absorption, photoluminescence and resonance Raman spectroscopy. The localization of the wavefunction can be obtained by mixing different k states with one another. The equation for making localized wavefunctions is called the Bethe–Salpeter equation.

Here, we show the Bethe–Salpeter equation for the tight-binding method in order to calculate the exciton energy Ω_n and the corresponding wavefunction Ψ^n [120,147,148,272,273]. Since the exciton wavefunction is localized in real space by a Coulomb interaction, the wavevector of an electron ($\mathbf{k}_\mathrm{c}$) or a hole ($\mathbf{k}_\mathrm{v}$) is not a good quantum number any more, and thus the exciton wavefunction Ψ_n for the nth exciton energy Ω_n is given by a linear combination of Bloch functions at many $\mathbf{k}_\mathrm{c}$ and $\mathbf{k}_\mathrm{v}$ wavevectors. In the case of carbon nanotubes, since the range of the Coulomb interaction is larger than the nanotube diameter, the mixed k's are selected near the k_ii point on one cutting line of the 1D BZ [148]. The mixing of different wavevectors by the Coulomb interaction is obtained by the Bethe–Salpeter equation [147]

$$\sum_{\mathbf{k}_\mathrm{c}\mathbf{k}_\mathrm{v}} \{[E(\mathbf{k}_\mathrm{c}) - E(\mathbf{k}_\mathrm{v})]\delta_{\mathbf{k}'_\mathrm{c}\mathbf{k}_\mathrm{c}}\delta_{\mathbf{k}'_\mathrm{v}\mathbf{k}_\mathrm{v}} + K(\mathbf{k}'_\mathrm{c}\mathbf{k}'_\mathrm{v}, \mathbf{k}_\mathrm{c}\mathbf{k}_\mathrm{v})\}\Psi^n(\mathbf{k}_\mathrm{c}\mathbf{k}_\mathrm{v}) = \Omega_n \Psi^n(\mathbf{k}'_\mathrm{c}\mathbf{k}'_\mathrm{v}), \tag{49}$$

where $E(\mathbf{k}_\mathrm{c})$ and $E(\mathbf{k}_\mathrm{v})$ are the quasi-electron and quasi-hole energies, respectively (see Equation (52)). Here "quasi-particle" means that the particle has a finite lifetime in an excited state because of the Coulomb interaction. Equation (49) is solved by a matrix that includes many

$\mathbf{k}'_{\mathrm{c}}$ and $\mathbf{k}'_{\mathrm{v}}$ points. The mixing term of Equation (49) which we call the kernel, $K(\mathbf{k}'_{\mathrm{c}}\mathbf{k}'_{\mathrm{v}}, \mathbf{k}_{\mathrm{c}}\mathbf{k}_{\mathrm{v}})$, is given by

$$K(\mathbf{k}'_{\mathrm{c}}\mathbf{k}'_{\mathrm{v}}, \mathbf{k}_{\mathrm{c}}\mathbf{k}_{\mathrm{v}}) = -K^{\mathrm{d}}(\mathbf{k}'_{\mathrm{c}}\mathbf{k}'_{\mathrm{v}}, \mathbf{k}_{\mathrm{c}}\mathbf{k}_{\mathrm{v}}) + 2\delta_{\mathrm{S}}K^{\mathrm{x}}(\mathbf{k}'_{\mathrm{c}}\mathbf{k}'_{\mathrm{v}}, \mathbf{k}_{\mathrm{c}}\mathbf{k}_{\mathrm{v}}) \tag{50}$$

with $\delta_{\mathrm{S}} = 1$ for spin singlet states and 0 for spin triplet states [167]. The direct and exchange interaction kernels K^{d} and K^{x} are, respectively, given by [274]

$$\begin{aligned} K^{\mathrm{d}}(\mathbf{k}'_{\mathrm{c}}\mathbf{k}'_{\mathrm{v}}, \mathbf{k}_{\mathrm{c}}\mathbf{k}_{\mathrm{v}}) &\equiv W(\mathbf{k}'_{\mathrm{c}}\mathbf{k}_{\mathrm{c}}, \mathbf{k}'_{\mathrm{v}}\mathbf{k}_{\mathrm{v}}) \\ &= \int \mathrm{d}\mathbf{r}'\,\mathrm{d}\mathbf{r}\,\psi^{*}_{\mathbf{k}'_{\mathrm{c}}}(\mathbf{r}')\psi_{\mathbf{k}_{\mathrm{c}}}(\mathbf{r}')w(\mathbf{r}',\mathbf{r})\psi_{\mathbf{k}'_{\mathrm{v}}}(\mathbf{r})\psi^{*}_{\mathbf{k}_{\mathrm{v}}}(\mathbf{r}), \\ K^{\mathrm{x}}(\mathbf{k}'_{\mathrm{c}}\mathbf{k}'_{\mathrm{v}}, \mathbf{k}_{\mathrm{c}}\mathbf{k}_{\mathrm{v}}) &= \int \mathrm{d}\mathbf{r}'\,\mathrm{d}\mathbf{r}\,\psi^{*}_{\mathbf{k}'_{\mathrm{c}}}(\mathbf{r}')\psi_{\mathbf{k}'_{\mathrm{v}}}(\mathbf{r}')v(\mathbf{r}',\mathbf{r})\psi_{\mathbf{k}_{c}}(\mathbf{r})\psi^{*}_{\mathbf{k}_{v}}(\mathbf{r}), \end{aligned} \tag{51}$$

where the functions w and v are the screened and bare Coulomb potentials, respectively, and ψ denotes the quasi-particle wavefunction. The quasi-particle energies are the sum of the single particle energy ($\epsilon(\mathbf{k})$) and the self-energy ($\Sigma(\mathbf{k})$),

$$E(\mathbf{k}_{\mathrm{i}}) = \epsilon(\mathbf{k}_{\mathrm{i}}) + \Sigma(\mathbf{k}_{\mathrm{i}}) \quad (i = \mathrm{c}, \mathrm{v}), \tag{52}$$

where the self-energy $\Sigma(\mathbf{k})$ is expressed by

$$\begin{aligned} \Sigma(\mathbf{k}_{\mathrm{c}}) &= -\sum_{\mathbf{q}} W(\mathbf{k}_{\mathrm{c}}(\mathbf{k}+\mathbf{q})_{\mathrm{v}}, (\mathbf{k}+\mathbf{q})_{\mathrm{v}}\mathbf{k}_{\mathrm{c}}), \\ \Sigma(\mathbf{k}_{\mathrm{v}}) &= -\sum_{\mathbf{q}} W(\mathbf{k}_{\mathrm{v}}(\mathbf{k}+\mathbf{q})_{\mathrm{v}}, (\mathbf{k}+\mathbf{q})_{\mathrm{v}}\mathbf{k}_{\mathrm{v}}). \end{aligned} \tag{53}$$

In order to determine the kernel and self-energy, the single particle Bloch wavefunction $\psi_{\mathbf{k}}(\mathbf{r})$ and the screening potential W are evaluated by either a first-principles calculation [147] or by using an extended tight-binding wavefunction within a random phase approximation (RPA) calculation [148]. In the RPA, the static screened Coulomb interaction for π electrons is expressed by

$$W = \frac{V}{\kappa\epsilon(\mathbf{q})}, \tag{54}$$

with a static dielectric constant κ and a dielectric function $\epsilon(\mathbf{q}) = 1 + v(\mathbf{q})\Pi(\mathbf{q})$. For describing the exciton energy and exciton wavefunction it is essential to select a reasonable function for the unscreened Coulomb potential $v(\mathbf{q})$ [120,148]. For 1D materials, the Ohno potential is commonly used for the unscreened Coulomb potential $v(q)$ for π orbitals [275] at two sites, $\mathbf{R}_{u's'}$ and $\mathbf{R}_{0s}$, (u: unit cell, s: atom position) with

$$v(|\mathbf{R}_{u's'} - \mathbf{R}_{0s}|) = \frac{U}{\sqrt{((4\pi\epsilon_0/e^2)U|\mathbf{R}_{us} - \mathbf{R}_{0s'}|)^2 + 1}}, \tag{55}$$

where U is the energy cost to place two electrons on a single site ($|\mathbf{R}_{us} - \mathbf{R}_{os'}| = 0$) and this energy cost is taken as $U \equiv U_{\pi_a\pi_a\pi_a\pi_a} = 11.3\,\mathrm{eV}$ for π orbitals [275]. The Ohno potential works well in reproducing the ground state and low-energy electronic excitations [276].

3.5.2. *Exciton–photon matrix element*

The exciton–photon matrix element $M_{\text{ex-op}}$ is given by a linear combination of the electron–photon matrix element $D_{\mathbf{k}}$ at $\mathbf{k}$, weighted by $Z^{n*}_{\mathbf{k}c,\mathbf{k}v}$

$$M_{\text{ex-op}} = \langle \Psi^n_0 | H_{\text{el-op}} | 0 \rangle = \sum_{\mathbf{k}} D_{\mathbf{k}} Z^{n*}_{\mathbf{k}c,\mathbf{k}v}, \tag{56}$$

where Ψ^n_0 is the exciton wavefunction with a $\mathbf{q} = 0$ center of mass momentum. Since the center of mass momentum is conserved before and after an optical transition, only $\mathbf{q} = 0$ excitons can be excited.

In the case of a SWNT, since the lattice structure is symmetric under a C_2 rotation around an axis which is perpendicular to the nanotube axis and goes through the center of a C–C bond, the C_2 exchange operation between A and B carbon atoms in the hexagonal lattice is equivalent to the exchange of $\mathbf{k}$ and $-\mathbf{k}$ states. Since the exciton wavefunction of a carbon nanotube should transform as an irreducible representation of the C_2 symmetry operation, we can get A_1, A_2, E and E^* symmetry excitons [142]. For example, the A_1 and A_2 exciton wavefunctions which are, respectively, symmetric and antisymmetric under a C_2 rotation, are given by

$$|\Psi^n_0(A_{1,2})\rangle = \frac{1}{\sqrt{2}} \sum_{\mathbf{k}} Z^n_{\mathbf{k}c,\mathbf{k}v} (c^+_{\mathbf{k}c} c_{\mathbf{k}v} \mp c^+_{-\mathbf{k}c} c_{-\mathbf{k}v}) |0\rangle, \tag{57}$$

where $\mathbf{k}$ and $-\mathbf{k}$ are located around the K and K' points, respectively, and $-(+)$ in $\mp$ corresponds to an A_1 (A_2) exciton.[19] When we use the relation $D_{\mathbf{k}} = D_{-\mathbf{k}}$, the excitonic-optical (ex-op) matrix elements for the A_1 and A_2 excitons are given by

$$\begin{aligned} M_{\text{ex-op}}(A^n_1) &= 0, \\ M_{\text{ex-op}}(A^n_2) &= \sqrt{2} \sum_{\mathbf{k}} D_{\mathbf{k}} Z^{n*}_{\mathbf{k}c,\mathbf{k}v}. \end{aligned} \tag{58}$$

Equation (58) directly indicates that A_1 excitons are dark and only A_2 excitons are bright, which is consistent with the predictions by group theory [277]. Because of the spatially localized exciton wavefunction, the exciton–photon matrix elements are greatly enhanced (on the order of 100 times) compared with the corresponding electron–photon matrix elements [273].

3.5.3. *The exciton–phonon interaction*

The exciton–phonon interaction is given by a linear combination of el–ph interactions weighted by the exciton wavefunction. Using creation and annihilation operators, the el–ph interaction for a phonon mode $(\mathbf{q}, \nu)$ is given by

$$H_{\text{el-ph}} = \sum_{\mathbf{kq}\nu} [M^{\nu}_{\mathbf{k},\mathbf{k}+\mathbf{q}}(c) c^+_{(\mathbf{k}+\mathbf{q})c} c_{\mathbf{k}c} - M^{\nu}_{\mathbf{k},\mathbf{k}+\mathbf{q}}(v) c^+_{(\mathbf{k}+\mathbf{q})v} c_{\mathbf{k}v}](b_{\mathbf{q}\nu} + b^+_{\mathbf{q}\nu}), \tag{59}$$

where $M(c)$ ($M(v)$) denotes the el–ph matrix element for the conduction (valence) band, and $b^+_{\mathbf{q}\nu}$ ($b_{\mathbf{q}\nu}$) is a phonon creation (annihilation) operator for the νth phonon mode at $\mathbf{q}$. From Equation (59), we obtain the exciton–phonon matrix element between the initial state $|\Psi^{n1}_{\mathbf{q}1}\rangle$ and a final state $|\Psi^{n2}_{\mathbf{q}2}\rangle$, by writing

$$M_{\text{ex}-\text{ph}} = \langle \Psi_{\mathbf{q}2}^{n2} | H_{\text{el-ph}} | \Psi_{\mathbf{q}1}^{n1} \rangle \\ = \sum_{\mathbf{k}} [M_{\mathbf{k},\mathbf{k}+\mathbf{q}}^{\nu}(c) Z_{\mathbf{k}+\mathbf{q},\mathbf{k}-\mathbf{q}1}^{n2*} Z_{\mathbf{k},\mathbf{k}-\mathbf{q}1}^{n1} - M_{\mathbf{k},\mathbf{k}+\mathbf{q}}^{\nu}(v) Z_{\mathbf{k}+\mathbf{q}2,\mathbf{k}}^{n2*} Z_{\mathbf{k}+\mathbf{q}2,\mathbf{k}+\mathbf{q}}^{n1}], \tag{60}$$

with $\mathbf{q} = \mathbf{q}_2 - \mathbf{q}_1$ accounting for momentum conservation. Since the electron–phonon interaction smoothly changes as a function of $\mathbf{k}$ for the region of the exciton wavefunction, the value of the exciton–phonon interaction is similar to the electron–phonon interaction [273].

3.6. *The resonance Raman process*

3.6.1. *Matrix elements for the resonance Raman process*

Combining all the matrix elements discussed above, we can formulate the first-order Stokes Raman intensity of graphene by time dependent perturbation theory as

$$I_{\text{el}} = \left| \frac{1}{L} \sum_{\mathbf{k}} \frac{D_{\mathbf{k}}^2 [M_{\text{el-ph}}(\mathbf{k} \to \mathbf{k}, c) - M_{\text{el-ph}}(\mathbf{k} \to \mathbf{k}, v)]}{[E - E_{\text{cv}}(\mathbf{k}) + \mathrm{i}\gamma][E - E_{\text{cv}}(\mathbf{k}) - E_{\text{ph}} + \mathrm{i}\gamma]} \right|^2, \tag{61}$$

where γ is the width of the resonance Raman window (Section 3.6.3) [278]. The γ value is essential in determining I_{el} as a function of laser excitation energy (Raman excitation profile). When we use the exciton–photon and exciton–phonon interactions, we apply the formula to the Raman intensity of SWNTs as follows:

$$I_{\text{ex}} = \left| \frac{1}{L} \sum_{a} \frac{M_{\text{ex-op}}(a) M_{\text{ex-ph}}(a \to b) M_{\text{ex-op}}(b)}{(E - E_a + \mathrm{i}\gamma)(E - E_a - E_{\text{ph}} + \mathrm{i}\gamma)} \right|^2 \\ = \left| \frac{1}{L} \sum_{a} \frac{M_{\text{ex-op}}(a)^2 M_{\text{ex-ph}}(a \to a)}{(E - E_a + \mathrm{i}\gamma)(E - E_a - E_{\text{ph}} + \mathrm{i}\gamma)} \right|^2. \tag{62}$$

In the second line of Equation (62), we assume that the virtual state b can be approximated by the real state a.[20] In the case of a first-order Raman process, since $\mathbf{q} = 0$, the matrix element of Equation (60) is simplified as

$$M_{\text{ex-ph}} = \sum_{\mathbf{k}} [M_{\mathbf{k},\mathbf{k}}^{\nu}(c) - M_{\mathbf{k},\mathbf{k}}^{\nu}(v)] |Z_{\mathbf{k},\mathbf{k}}|^2. \tag{63}$$

When we consider the second-order Raman intensity, we should consider $\mathbf{q} \neq \mathbf{0}$ phonon scattering. In this case, the exciton–phonon interaction between an A_2 exciton state and an E exciton state is important, in particular, for the case where the E exciton state consists of an electron near the K point and a hole near the K' point and vice versa. Here the inter-valley exciton–phonon interaction is generally large.

3.6.2. *Matrix elements for double resonance Raman scattering*

The two-phonon process is described in quantum mechanical terms by using fourth-order, time-dependent perturbation theory and the scattering intensity can be calculated using:

$$I(\omega, E_{\text{laser}}) \propto \sum_{i} \left| \sum_{m', m'', \omega_1, \omega_2} J_{m', m''}(\omega_1, \omega_2) \right|^2, \tag{64}$$

in which the summation is taken over two intermediate electronic states m and m' and the corresponding phonon frequencies ω_1 and ω_2 with phonon wavevectors $-q_1$ and $-q_2$, respectively, and for the initial states i, after taking the square of the scattering amplitude, $J_{m,m'}$ that is given by

$$J_{m',m''}(\omega_1,\omega_2) = \frac{M_{\text{ex-op}}(im'')M_{\text{ex-ph}}(m''m')M_{\text{ex-ph}}(m'm)M_{\text{ex-op}}(mi)}{(\Delta E_{m''i} - \hbar\omega_1 - \hbar\omega_2 - \mathrm{i}\gamma)(\Delta E_{m'i} - \hbar\omega_1 - \mathrm{i}\gamma)(\Delta E_{mi} - \mathrm{i}\gamma)}, \tag{65}$$

where $\Delta E_{m'i} \equiv E_{\text{laser}} - (E_m - E_{\text{i}})$ and $M_{\text{ex-op}}(mi)$ denote the optical transition from i to m states, etc. In general, energy and momentum conservation for the incident (i) and scattered (s) electrons requires:

$$E_{\text{s}} = E_{\text{i}} \pm E_{q1} \pm E_{q2}, \tag{66}$$

$$k_{\text{s}} = k_{\text{i}} \mp q_1 \mp q_2, \tag{67}$$

where + (−) in Equation (66) and − (+) in Equation (67) correspond to phonon absorption and emission with the wavevectors q_1 and q_2. By considering $k_{\text{s}} \approx k_{\text{i}}$ (see Section 1.5), momentum conservation requires $q_2 \approx -q_1$ for satisfying the DR condition for two of the three energy denominators in Equation (65).

3.6.3. *Resonance window width*

The resonance width, or γ in eV, of the Raman excitation profile is related by the uncertainty relation in quantum mechanics and to the lifetime of the photo-excited carriers. Usually, the dominant contribution to the lifetime of the carriers in the Raman spectra is in an inelastic scattering process by the emission or absorption of phonons. The Raman spectral width, Γ in cm^{-1}, in the Raman spectra, on the other hand, which has a different physical value from γ, is related to the phonon lifetime. Γ is determined by the elastic (or inelastic) scattering of a phonon due to defects, anharmonicity or by the electron–phonon interaction. The carrier transition rate τ ($=\hbar/\gamma$), [139,263,267,278] is estimated by the Fermi Golden rule for the electron–phonon matrix elements [268,269]. For metallic systems (graphene and M-SWNTs), an additional interaction of phonons with free electrons can shorten the lifetime (broaden the γ values) significantly, and this additional interaction is known as the Kohn anomaly (KA) (Section 3.6.5).

The transition rate $1/\tau$ or the scattering rate per unit time of an excited electron from an initial state $\mathbf{k}$ to all possible final states $\mathbf{k}'$ by the νth phonon mode is given by [263]

$$\begin{aligned}\frac{1}{\tau_\nu} &= W_{\mathbf{k}}^{\nu} \\ &= \frac{S}{8\pi M d_t}\sum_{\mu',k'}\frac{|D_\nu(\mathbf{k},\mathbf{k}')|^2}{\omega_\nu(\mathbf{k}'-\mathbf{k})}\left[\frac{\mathrm{d}E(\mu',k')}{\mathrm{d}k'}\right]^{-1} \\ &\quad\times\left\{\frac{\delta(\omega(\mathbf{k}')-\omega(\mathbf{k})-\omega_\nu(\mathbf{k}'-\mathbf{k}))}{\mathrm{e}^{\beta\hbar\omega_\nu(\mathbf{k}'-\mathbf{k})}-1}+\frac{\delta(\omega(\mathbf{k}')-\omega(\mathbf{k})+\omega_\nu(\mathbf{k}'-\mathbf{k}))}{1-\mathrm{e}^{-\beta\hbar\omega_\nu(\mathbf{k}'-\mathbf{k})}}\right\},\end{aligned} \tag{68}$$

where S, M, d_t, β and μ', respectively, denote the area of the graphene unit cell, the mass of a carbon atom, the diameter of a SWNT, $1/k_{\text{B}}T$ (where k_{B} is the Boltzmann constant), and the cutting line indices of the final state. Here $\mathrm{D}_\nu(\mathbf{k},\mathbf{k}')$ denotes a matrix for scattering an electron from $\mathbf{k}$ to $\mathbf{k}'$ by the νth phonon mode. The relaxation process is restricted to 24 possible phonon scattering processes satisfying energy–momentum conservation [267]. The two terms in braces in Equation (68), respectively, represent the absorption and emission processes of the νth phonon mode with energy $\hbar\omega_\nu(\mathbf{k}' - \mathbf{k})$. The calculation of the transition rates as in Equation (68) have been considered by the Ferrari group using another approach [151,219].

For the result, in the case of S-SWNTs, we can obtain calculated γ values in agreement with experiments by just considering the electron–phonon coupling model [278]. The calculated γ value shows a strong dependence on chirality and diameter for S-SWNTs. However, the calculated γ value for M-SWNTs is much smaller than the experimental γ value which shows the presence of

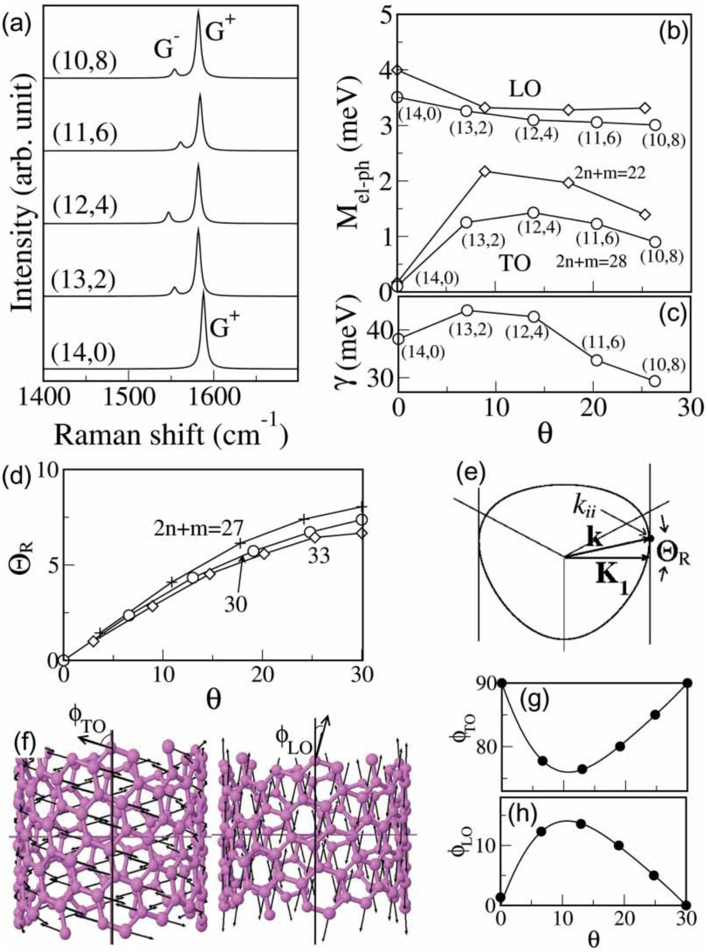

Figure 35. (a) The calculated G-band spectra for S-SWNTs with the same family number $p = 2n + m = 28$. (b) The calculated electron–phonon matrix elements vs. chiral angle θ for the LO and TO phonons and for two different $2n + m$ family numbers (22 and 28). (c) Plot of γ vs. θ for members of $p = 28$. (d) Plot of Θ_R vs. θ for three $2n + m$ families of M-SWNTs. (e) The angle Θ_R between the circumferential vector K_1 and the cutting line for the polar coordinate of a $\mathbf{k}$ vector at the van Hove singular point. (f) The angle ϕ between the tube axis and the phonon eigenvector direction for a (12,6) SWNT. The calculated angles ϕ vs. θ for the TO phonons (g) and the LO phonons. (h) For the results for the LO phonons as a function of θ (fitted by the function of Equation (70) (see text)). Reprinted with permission from J.S. Park *et al.*, Physical Review B 80, p. 81402, 2009 [86]. Copyright © (2009) by the American Physical Society.

an additional scattering path associated with the charge carriers in M-SWNTs. Such a scattering path might come from the electron–electron interaction, but this theory is not yet well described.

3.6.4. *G-band intensity for semiconducting SWNTs*

Next, we consider the G-band Raman intensity as a function of (n, m) [86]. Figure 35(a) shows the calculated resonance Raman spectra for the G-band for type I S-SWNTs [86] with family number $p = 2n + m = 28$. The (n, m) SWNTs with the same family number p have a similar diameter and E_{ii} value to one another. In this figure, values for E_{L} and γ (see Figure 35(c)) are taken from E^S_{22} for each (n, m) SWNT. The chiral angle can vary from $\theta = 0°$ to $\theta \sim 30°$. The intensity of the G$^-$ peak (TO) is always smaller than that of the G$^+$ peak (LO), because $\mathcal{M}^{\text{R,LO}}_{\text{ep}} > \mathcal{M}^{\text{R,TO}}_{\text{ep}}$ for the electron–phonon matrix elements, as shown in Figure 35(b), in which the above notation R indicates Raman scattering. In particular, the intensity of the G$^-$ peak vanishes for a (14,0) SWNT, since $\mathcal{M}^{\text{R,TO}}_{\text{ep}}$ for zigzag SWNTs is zero, as shown in Figure 35(b). Here $\mathcal{M}^{\text{R}}_{\text{ep}}$ is calculated for the phonon amplitude at 300 K. These calculated G-band Raman spectra can be compared with previous experimental results which show only one peak in the G-band spectra of (n, m) SWNTs with smaller chiral angles [193,279].

In order to explain the chiral angle dependence of the el–ph matrix elements for the LO and TO phonons, we obtain the analytical formulae for the el–ph matrix element within the effective mass approximation [196]

$$\begin{aligned} \mathcal{M}^{\text{R,LO}}_{\text{ep}} &\equiv \langle e(\mathbf{k}), \omega_{\text{LO}} | \mathcal{H}_{\text{ep}} | e(\mathbf{k}) \rangle = gu \cos \Theta_{\text{R}}(\mathbf{k}), \\ \mathcal{M}^{\text{R,TO}}_{\text{ep}} &\equiv \langle \text{e}(\mathbf{k}), \omega_{\text{TO}} | \mathcal{H}_{\text{ep}} | \text{e}(\mathbf{k}) \rangle = -gu \sin \Theta_{\text{R}}(\mathbf{k}), \end{aligned} \tag{69}$$

respectively, where g is the el–ph coupling constant, u the phonon amplitude and $\Theta_{\text{R}}(\mathbf{k})$ is defined by an angle between the $\mathbf{k}$ vector from the K point of the 2D BZ to the van Hove singular point, k_{ii}, and the circumferential direction vector, $\mathbf{K}_1$, [32,136,177] as shown in Figure 35(d). The values of g are consistent with the work by Basko *et al.* [151,219]. Since $\Theta_{\text{R}}(\mathbf{k})$ is zero for all zigzag SWNTs $(\mathbf{k} \parallel \mathbf{K}_1)$, we obtain $\mathcal{M}^{\text{R,TO}}_{\text{ep}} = 0$, while $\mathcal{M}^{\text{R,LO}}_{\text{ep}}$ has a maximum value [196]. The meaning of Θ_{R} vs. θ for SWNTs with the same family number p is shown in Figure 35(e). For the TO phonon mode, the magnitude of the matrix element $\mathcal{M}^{\text{R}}_{\text{ep}}$ for SWNTs with a similar θ value increases with decreasing d_{t} because of the diameter dependence in the circumferential direction [86] as shown in Figure 35(b). The angle ϕ between the SWNT- axis and the phonon eigenvector for the LO and TO phonons [280] is essential for determining the value of the el–ph matrix element. In fact, when we consider ϕ, then Equation (69) is modified and becomes

$$\begin{aligned} \langle e(\mathbf{k}), \omega_{\text{LO}} | \mathcal{H}_{\text{ep}} | e(\mathbf{k}) \rangle &= gu \cos(\Theta_{\text{R}}(\mathbf{k}) + \phi), \\ \langle \text{e}(\mathbf{k}), \omega_{\text{TO}} | \mathcal{H}_{\text{ep}} | \text{e}(\mathbf{k}) \rangle &= -gu \sin(\Theta_{\text{R}}(\mathbf{k}) + \phi). \end{aligned} \tag{70}$$

Figure 35(g) and (h) show that the calculated angle ϕ here changes smoothly as a function of θ [86]. The sum $\phi_{\text{LO}} + \phi_{\text{TO}}$ for a general chiral angle θ always becomes $\pi/2$, because of symmetry. The angle ϕ vs. θ for the LO and TO phonons can be fitted by the chiral angle dependence $(A + B\theta + C\theta^2)\sin(6\theta)$, where A, B and C are fitting parameters and θ is the chiral angle in units of degrees (°). Values obtained for A, B and C for ϕ_{LO}, are $A = 26.9, B = -76.3$ and $C = 84.5$, respectively, and for ϕ_{TO}, the corresponding values are $A = -26.7, B = 75.4$, and $C = -83.2$. The units for the fitting parameters are degree (°). This ϕ dependence of ϕ_{LO} and ϕ_{TO} should be taken into account when carrying out Raman spectral calculations.

3.6.5. *G-band intensity for metallic SWNTs: The Kohn Anomaly*

In the case of metallic SWNTs, the G-band spectra become soft and broad and they are represented by the Breit–Wigner–Fano (BWF) lineshape [128]. The BWF lineshape has been widely observed for graphite intercalation compounds as a function of doping concentration and also as a function of carrier density [281]. The phonon softening phenomena for metallic SWNTs is understood by the electron–phonon interaction between phonons and free electrons at the Fermi energy, ($E_{\rm F}$), and these phenomena are known as the KA effect [127] which has been widely discussed [151,193,194,197–199,243]

The phonon frequency ω of the LO and TO phonon modes at the Γ point for M-SWNTs is modified by the KA effect, which we understand by second-order perturbation theory. The phonon energy $\hbar\omega$ becomes $\hbar\omega = \hbar\omega^{(0)} + \hbar\omega^{(2)}$, where $\omega^{(0)}$ is the original phonon frequency without the el–ph interaction, and $\omega^{(2)}$ is the quantum correction to $\omega^{(0)}$ which is given by [196]

$$\begin{aligned}\hbar\omega^{(2)} = 2\sum_{\mathbf{k}} & \frac{|\langle \mathrm{eh}(\mathbf{k})|\mathcal{H}_{\rm ep}|\omega^{(0)}\rangle|^2}{\hbar\omega^{(0)} - [E_e(\mathbf{k}) - E_h(\mathbf{k})] + i\Gamma} \\ & \times \{f[E_e(\mathbf{k}) - E_{\rm F}] - f[E_h(\mathbf{k}) - E_{\rm F}]\},\end{aligned} \tag{71}$$

in which the factor 2 comes from spin degeneracy, and $E_e(\mathbf{k})$ [$E_h(\mathbf{k})$] denotes the electron (hole) energy as a function of wave vector $\mathbf{k}$, while $\langle eh(\mathbf{k})|\mathcal{H}_{\rm ep}|\omega^{(0)}\rangle$ represents the el–ph matrix element for creating an e–h pair with wave number $\mathbf{k}$ by the el–ph interaction $\mathcal{H}_{\rm ep}$ and $f(E)$ is the Fermi distribution function. The G-band spectral width is given by the decay width Γ in Equation (71), which is calculated self-consistently by evaluating $\Gamma = -\mathrm{Im}(\hbar\omega^{(2)})$ [196,205]. The electron–phonon interaction is used, too, for defining the $\omega^{(0)}$ and thus we should be careful about not double counting the constituents of this interaction [198].

Figure 36(a) shows the calculated Raman spectra for the G-band of M-SWNTs with family number $p = 30$ and $E_{\rm F}$=0. The $E_{\rm L}$ and γ values (see Figure 36(c)) are taken from E_{11}^M for each (n, m) SWNT. The G^- peak intensity is larger than that of the G^+ peak, because the G^- (G^+) peak corresponds to the LO (TO) phonon due to the LO phonon softening, in which $\mathcal{M}_{\rm ep}^{\rm R,LO} > \mathcal{M}_{\rm ep}^{\rm R,TO}$ for any θ value, as shown in Figure 36(b). The relative intensities of the two peaks, G^+ and G^-, are affected by the Raman spectral width which relates to the phonon lifetime, Γ. For the (10,10) armchair SWNT, the G^+ (TO) peak width is significantly smaller than those for the G^- (LO) peak

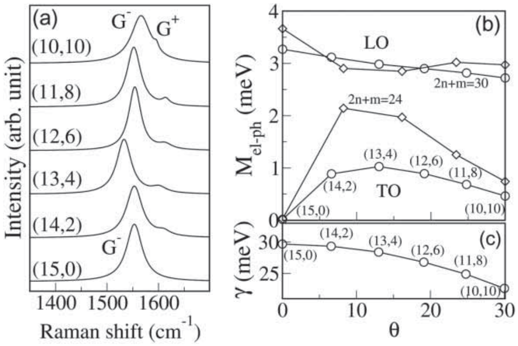

Figure 36. (a) The calculated G-band spectra of M-SWNTs with the same family number $p = 30$ and $E_{\rm F}$=0. (b) el–ph matrix elements vs. θ for the LO and TO phonons and for two different $2n + m$ family numbers. Open-circles indicate the $\mathcal{M}_{\rm ep}$ values for the family number $p = 30$. (c) γ vs. θ for members of $p = 30$. Reprinted with permission from J.S. Park *et al.*, Physical Review B 80, p. 81402, 2009 [86]. Copyright © (2009) by the American Physical Society.

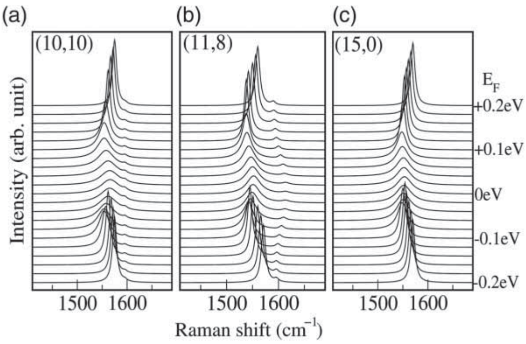

Figure 37. The calculated G-band spectra for three M-SWNTs with different chiral angles taken by changing the Fermi energy from $E_{\mathrm{F}} = -0.2$ eV to 0.2 eV. (a) (10,10). (b) (11,8) and (c) (15,0). Reprinted with permission from J.S. Park *et al.*, Physical Review B 80, p. 81402, 2009 [86]. Copyright © (2009) by the American Physical Society.

and of the G^+ peaks for the other chiral tubes. Therefore, the G^+ peak intensity of the (10,10) tube becomes large compared with the other chiral SWNTs, even though the $\mathcal{M}_{\mathrm{ep}}^{\mathrm{R,TO}}$ for the armchair tube has a smaller value than that for the other chiral tubes. Since the Raman peak intensity is large for large $\mathcal{M}_{\mathrm{ep}}$ and small Γ values, the chiral angle dependence of these values gives an irregular behavior to the G^+/G^- spectra as a function of (n, m), as seen in Figure 36.

For a zigzag SWNT $((15, 0))$, only the G^+ peak appears, because $\mathcal{M}_{\mathrm{ep}}^{\mathrm{R,TO}}$ vanishes for zigzag nanotubes as seen in Equation (69). The other chiral tubes in this $p = 2n + m > 30$ family, (11,8), (12,6), (13,4) and (14,2), show various intermediate intensity ratios. In Figure 36(c), we show that γ decreases monotonically with increasing θ. Because of the small difference between the γ and the el–ph coupling for the LO phonon as compared to that for the TO phonon as a function of θ, the G^- peak intensity does not show a large change for the different chiral SWNTs. These results show that the G-band intensity for both the G^+ and G^- components depends on θ, but the Raman intensity is more sensitive to the E_{F} position, especially for M-SWNTs.

This effect is shown more clearly by varying the Fermi Level, as shown in Figure 37(a), where the calculated G-band spectra is plotted vs. E_{F} at 300 K for a (10,10) armchair SWNT. Here neither are the changes in the C–C bond nor the changes in the E_{ii} transition energy by doping with electrons or holes considered [86].

In Figure 37, the positive (negative) Fermi energy $+E_{\mathrm{F}}$ $(-E_{\mathrm{F}})$ corresponds to electron (hole) doping. When E_{F} is changed from $E_{\mathrm{F}} = 0$, the G^- peak shows a frequency shift and a sharpening of the spectral width, while the G^+ peak does not show any change in intensity or width. The el–ph interaction for the photo-excited electron does not couple to the TO phonon for armchair SWNTs [196]. For the chiral M-SWNT (11,8) as shown in Figure 37(b), both the LO and TO phonons couple to the intermediate e–h pair state, which is excited by a lower energy phonon. The TO phonon becomes harder for $E_{\mathrm{F}} = 0$ eV, since the intermediate state of an e–h pair for $E < \hbar\omega_{\mathrm{TO}}$ contributes to a TO phonon hardening [196]. In the case of the (15,0) SWNT, the G^+ peak always vanishes because of a vanishing $\mathcal{M}_{\mathrm{ep}}^{\mathrm{R,TO}}$ (See Figure 36(b)).

The matrix element $\mathcal{M}_{\mathrm{ep}}^{\mathrm{KA}}$ for the KA effect in Equation (71) is given by [196]

$$\begin{aligned}
\mathcal{M}_{\mathrm{ep}}^{\mathrm{KA,LO}} &\equiv \langle \mathrm{eh}(\mathbf{k}) | \mathcal{H}_{\mathrm{ep}} | \omega_{\mathrm{LO}} \rangle = \mathrm{i}gu \sin \Theta_{\mathrm{KA}}(\mathbf{k}), \\
\mathcal{M}_{\mathrm{ep}}^{\mathrm{KA,TO}} &\equiv \langle \mathrm{eh}(\mathbf{k}) | \mathcal{H}_{\mathrm{ep}} | \omega_{\mathrm{TO}} \rangle = -\mathrm{i}gu \cos \Theta_{\mathrm{KA}}(\mathbf{k}),
\end{aligned} \tag{72}$$

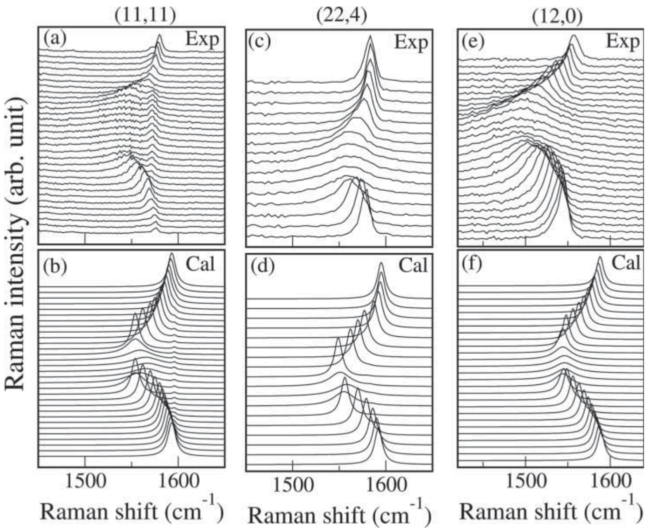

Figure 38. (a,c,e) Experimental G-band Raman spectra which are given by the electro-chemical doping effect. (a) $V_g = 1.5$ to -1.5 V. (c) $V_g = 1.9$ to -1.3 V. (e) $V_g = 1.3$ to -1.3 V with the traces taken at uniform changes in V_g. (b,d,f) Calculated G-band Raman spectra taken by changing the Fermi energy E_F in equal steps (b) 0.45 to -0.45 eV, (d) 0.60 to -0.42 eV and (f) 0.39 to -0.39 eV. The tube chiralities are: (a,b) (11,11), (c,d) (24,4) and (e,f) (12,0). Reprinted with permission from J.S. Park *et al.*, Physical Review B 80, p. 81402, 2009 [86]. Copyright © (2009) by the American Physical Society.

where $\Theta_{KA}(\mathbf{k})$ is defined as the angle between the **k** point taken on a cutting line[21] for two-linear metallic sub-bands and the nanotube circumferential direction of a unit vector, $\mathbf{K}_1$. For the armchair nanotube, the cutting line for the two-linear metallic bands lies on the nanotube axis direction unit vector, and then Θ_{KA} is $\pi/2$ $(-\pi/2)$, which gives a vanishing $\mathcal{M}_{ep}^{KA,TO}$. For a chiral nanotube, Θ_{KA} is not zero, since the cutting line for the two-linear metallic bands deviates from the K point due to the curvature effect, and then the KA effect appears in both the LO and TO modes. For the zigzag M-SWNT (15,0), only the G^- peak that is related to the LO phonon appears, since the el–ph matrix element for the Raman scattering process for iTO phonon has a zero value for a zigzag tube, as shown in Figure 36(b). Thus, only an LO phonon softening is measured experimentally, even though a TO phonon hardening was expected theoretically.

The calculated G-band Raman spectra vs. E_F can be directly compared with the experimental G-band Raman spectra which are obtained for electro-chemically doped individual SWNTs, as seen in Figure 38 [86]. Here, we assume $\Delta E_F = 0.3\Delta V_g$ according to Sasaki *et al.* [196]. The experimental Raman spectra are shown in Figure 38(a,c,e), and the corresponding calculated Raman spectra are shown in Figure 38(b,d,f). In Figure 38(a), the experimental Raman spectra show only a LO phonon softening, and a TO phonon frequency shift does not occur. As mentioned above, for the armchair SWNT, the TO phonon frequency shift does not appear and only LO phonon softening appears. Therefore, we can predict that Figure 38(a) shows an armchair-type behavior by changing the gate voltage. The RBM peak for these experimental Raman spectra appears at 161 cm^{-1} with $E_L = 1.72$ eV. Then we can select possible (n, m) values for a tube by using a simple tight-binding (STB) model with $\gamma_0 = 2.9$ eV for simplicity and by using the relation between the RBM frequency and diameter, $\omega_{RBM}(\text{cm}^{-1}) = 248/d_t(\text{nm})$[22], the possible for identifying the possible (n, m) values for SWNTs we obtain these (n, m) values as (19,1), (18,3), (14,8) and (11,11). If our prediction is correct, Figure 38(a) can be assigned as an (11,11) armchair SWNT. Figure 38(c) and (e) are assigned as chiral (24,4) and zigzag (12,0) SWNTs, respectively, from the possible (n, m) values, {(21, 6), (22, 4), (23, 2)} and {(10, 4), (11, 2), (12, 0)}. For the chiral M-SWNTs, not only is there a LO phonon softening, but there is also a TO phonon hardening that appears in the calculation of the G-band Raman spectra vs. E_F. However, in Figure 38, the TO peak is too small to see on the intensity scale of the figure. Figure 38(e) shows that the zigzag SWNT has only a G^- peak and thus only the LO phonon softening appears by changing E_F, experimentally. Brown *et al.* [128] and others [282,283] pointed out that asymmetric line shapes appear in the G^- band Raman spectrum for metallic tubes, which is related to the Fano resonance (Breit–Wigner–Fano, BWF line shape) lines. Recently, Farhat *et al.* showed that this asymmetry is sensitive to the relative position of the scattered light energy relative to $E_{ii}^{(M)}$, suggesting that the electron–electron interaction is important for understanding BWF lineshapes [206].

4. Raman spectra of graphene

In the family of sp^2 carbon systems, mono-layer graphene is the simplest crystal structure (see Figure 2), having the highest symmetry and, consequently, the simplest Raman spectra (see Figure 39). The big rush into graphene research started in 2004 [7,55,61]. The large research community that had become knowledgeable about the Raman spectroscopy associated with other nano-carbon systems was ready for a quick appreciation of the Raman spectra in mono-layer graphene as a perfect prototype spectra for the study and characterization of sp^2 carbons more generally [112,114,250]. For example, the detailed study of effects of inter-layer coupling on the *electronic* structure was carried out using the dispersion of the G′-band when changing the excitation laser energy in bi-layer graphene [284]. Strain[285–287], charge transfer and disorder effects due to doping, top gates and different types of substrates were addressed using the G and G′-bands of graphene [151,191,192,195,284–291]. Actually, graphene provides an ideal system to study defects using light as a probe because there are no aspects related to the penetration depth [3,65,292]. Interestingly, most of these findings in graphene are helping our basic understanding of long standing experimental results on carbon nanotubes and other nanocarbon systems [151,191,192,195,288,289,293]. Another important aspect that is peculiar to graphene is the fact that the G-band phonons (energy of 0.2 eV) can promote electrons from the valence band to the conduction band. This happens because graphene is a zero gap semiconductor, and the linear $E(k)$ dispersion relation centered around the Dirac cones for the valence and conduction bands (see Figure 9(a)) near the Fermi level makes the effect especially interesting, and it gives rise to a

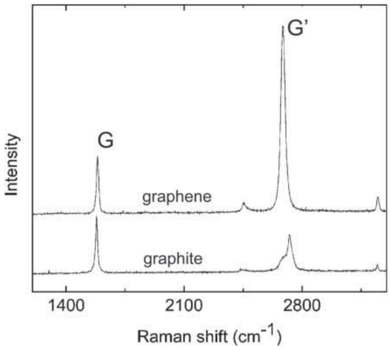

Figure 39. Raman spectrum of single-layer graphene in comparison to graphite measured with a $E_{laser} = 2.41$ eV (514 nm) laser. The two most intense features are named the G and G′-bands. The Raman spectrum of pristine mono-layer graphene is unique among sp^2 carbons, i.e., the second-order G′ feature is very intense when compared to the first-order G-band feature (see discussion in Section 4.1) [112,250].

renormalization of the electronic and phonon energies, including a sensitive dependence of the electronic structure on electron or hole doping [195]. Raman imaging can be used to define the number of layers in different locations of a given graphene flake by measuring the dependence of the Raman spectra (e.g., for the G-band intensity) on the number of scattering graphene layers [294]. It is true that such information has to be analyzed with care since doping and other physical phenomena perturb the graphene Raman spectra. The effect of environmental interactions on few-layer graphene samples have also been studied using Raman spectroscopy, including the epitaxial growth of graphene on a substrate [295]. In this brief survey a number of important topics are reviewed, including the spectra of mono-layer graphene, the layer number dependence in few layer graphene, disorder-related phenomena, edge phonon phenomena, polarization effects and the effects of doping.

4.1. *The G-band and G′-band intensity ratio*

The first intriguing result that was observed when the Raman spectrum from single layers of graphene was measured was the unusual G′ to G intensity ratio $I_{G'}/I_G$. While the second-order G′ Raman band in 3D graphite has a much smaller intensity than the first-order Raman-allowed G-band, in single-layer graphene the G′-band intensity is much stronger, reaching 4 times the G-band intensity. In principle, the G′ to G intensity ratio can be used to determine the number of layers in a few layer graphene sample, since $I_{G'}/I_G$ is reduced by increasing the number of layers. However, it is also true that this ratio is sensitive to doping [220,291] and disorder [130], and the intermixing of information (doping vs. number of layers) makes it complicated to use Raman spectroscopy to determine the number of layers in few-layer graphene samples accurately, unless the parameters for the environmental effects are clearly delineated.

Basko [219,296] argues that the special Raman spectrum of mono-layer graphene (1-LG) is an indication that the very strong G′-band comes from a fully resonant scattering process where both the el–ph absorption and emission are resonant, as well as the el–ph and hole–phonon scattering processes, so that the absorption and recombination occur at different Dirac cones. The very strong G′-band intensity could also be related to different el–ph matrix elements near the K point (for the G′-band) and near the Γ point (for the G-band) phonons [218–220]. The fully resonant process should, in principle, be much more probable than the other processes which exhibit a virtual (non-resonant) state. However, this can only happen if the electron and hole electronic dispersion relations are symmetric within the phonon uncertainty and if the electron and hole scattering by phonons is equally probable. Since the electron wave function overlap in graphene results in a different normalization for the valence and conduction bands, an e–h dispersion asymmetry is introduced, and for this reason the two processes could select double resonance phonons with somewhat different q vectors. This asymmetry is relatively small and is generally neglected in common descriptions of the electronic structure of graphene in terms of mirror band cones. More theoretical and experimental work is required to fully understand the differences in the el–ph vs. hole–phonon scattering, including the differences in the matrix elements for these two processes.

4.2. *Layer number dependence of G′-band*

4.2.1. *The number of graphene layers with AB stacking*

Because of its dependence on the layer number, the Raman G′-band has been used to characterize the number of layers in few layer graphene samples and the stacking order between these layers, as shown in Figure 40. The Raman spectra for highly ordered pyrolytic graphite (HOPG) and for turbostratic graphite (which has random inter-layer stacking) are also shown in Figure 40 for comparison. To explain this observed behavior, we first remind the reader about the dispersive

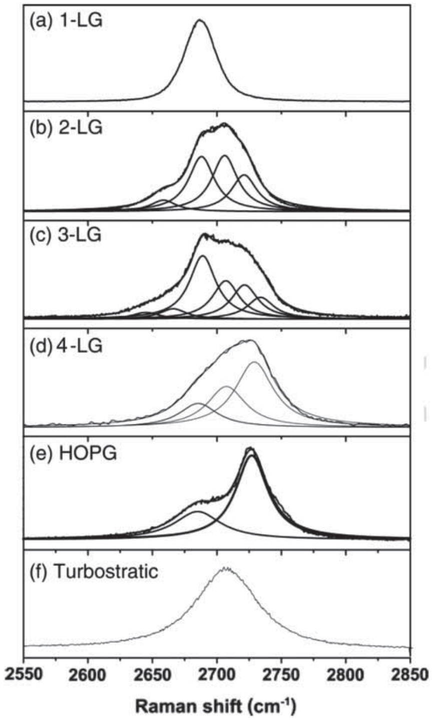

Figure 40. The differences in the G′ Raman band for (a) 1-LG, (b) 2-LG, (c) 3-LG, (d) 4-LG, (e) HOPG and (f) turbostratic graphite. All spectra are measured with $E_{\text{laser}} = 2.41$ eV. The original work was done by Ferrari *et al.* [112] and is summarized in the review article of Malard *et al.* [5].

behavior discussed in connection with Figures 24 and 27. Then we turn to a discussion of the electronic properties of bi-layer graphene with AB Bernal layer stacking (as also occurs in graphite), since the band structure change from mono-layer to bi-layer graphene is the most striking and both mono-layer and bi-layer graphene have been probed by Raman scattering [284]. The change in the electronic structure of graphene due to layer stacking can be probed in some detail by the DR Raman features (see Section 3.1.3), and most sensitively by the detailed lineshape of the G′-band [112]. Bi-layer graphene has a 4-peak G′-band spectrum (Figure 40(b)) while mono-layer has a 1-peak G′-band (Figure 40(a)), and this fact is explained by the special electronic structure of bi-layer graphene, which consists of two conduction and two valence bands [112], as discussed below.

Figure 41(a) shows the dispersion (peak frequency as a function of E_{laser}) of each one of the four peaks in Figure 40(b), which comprises the G′-band for bi-layer graphene with AB stacking. The double Raman resonance processes for bi-layer graphene are shown in Figure 41(b)–(e), where the diagrams show the possible DR Raman processes that give rise to the four G′ peaks in Figure 41(a). The processes are labeled by P_{ij} $(i, j = 1, 2)$ [284], where the states with energy E_{i} in the valence band and E_j in the conduction band are connected in the photon absorption process using laser energy E_{laser}. The highest frequency G′ peak for a given E_{laser} energy is associated with the P_{11} process, since the P_{11} process has the largest wave vector (q_{11}) and the iTO phonon along the KM direction in the BZ increases its frequency with increasing wave vector q (see Figure 40(b) and Figure 41). The lowest frequency G′-band peak is associated with the process P_{22}, which gives rise to the smallest phonon wave vector q_{22}. Processes P_{12} and P_{21} shown in Figure 41(b) give rise to the two intermediate frequency peaks of the G′-band [112,284,297]. This DR Raman model has been used to relate the electronic and phonon dispersion of bi-layer graphene with the experimental dependence of $\omega_{G'}$ on E_{laser} [284].

Tri-layer graphene has 15 possible DR processes [1,4], but the frequency spacings between these peaks are not large enough to allow identification of each of the 15 scattering events (Figure 40(c)). Increasing the number of layers increases the number of possibilities for the G′-band DR scattering processes, and an in depth analysis would get more and more complicated for N-layer graphene ($N > 3$). However, experimentally the G′-band spectra at a typical E_{laser} energy (e.g., 2.41 eV) actually gets simpler in appearance when the number of layers increases (see, for example Figure 40(d) for 4-LG). The spectra of increasing N converge to the two-peak structure observed in HOPG, where $N \to \infty$, as shown in Figure 40(e). The two-peak structure of HOPG (Figure 40(e)) is the result of a 3D electron and phonon dispersion, as discussed in [298], which can be seen as a convolution of an infinite number of allowed DR processes along the third dimension of $N \to \infty$ graphite.

4.2.2. *Characterization of the graphene stacking order by the G′ spectra*

The use of G′-band Raman spectroscopy to assign the number of layers has to be a cautious procedure, because the G′-band lineshape is related not only to the number of layers, but also to the stacking order of these layers. The G′-band has actually been used to quantify the structural ordering along the *c*- axis in graphite [299–301] much before the rise of the graphene field in 2004. The change from one peak to two peaks in the G′-band profile observed in the Raman spectra from polycrystalline to crystalline graphite was shown in the late 1970s [223,302]. Raman spectroscopy studies of carbon materials heat treated at different temperatures T_{htt}[23] show that, by increasing T_{htt}, the G′-band changes from a one-peak to a two-peak structure (see Figure 40(e,f)) [299,300]. Lespade *et al.* [299] associated this evolution with the degree of graphitization of the samples, suggesting that the origin of the two-peak structure of the G′-band in crystalline graphite was related to the stacking order occurring along the *c*- axis. Finally, the evolution from the 2D to 3D aspect (from one to two peaks [303]) has been quantitatively systematized (see also Section 4.2.1). Barros *et al.* have used the G′-band to identify three G′-band peaks due to the coexistence of 2D

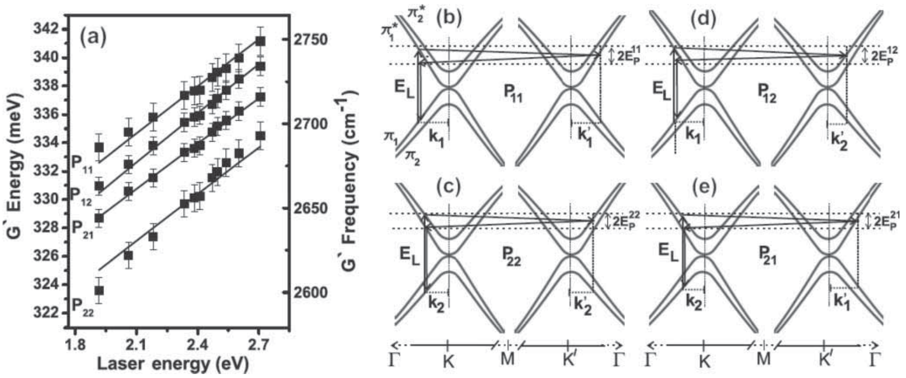

Figure 41. (a) Plot of the frequency of the four Raman G′-band peaks vs. E_{laser} observed in bi-layer graphene. These four peaks arise from the four processes shown in (b)–(e) which comprise the G′-band scattering processes that are expected for the phonon frequencies in bi-layer (2-LG) graphene plotted in (a) as a function of laser energy E_{laser}. Reprinted with permission from L.M. Malard *et al.*, Physical Review B 76, p. 201401, 2007 [284]. Copyright © (2007) by the American Physical Society.

and 3D graphite phases in more complicated carbon-based materials, such as pitch-based graphitic foams [101].

The differences between stacked and non-stacked graphene layers became even more clear when the G-band Raman spectra of AB stacked and misoriented folded bi-layer graphene were compared [4,295,304]. While the AB stacked bi-layer graphene shows a four-peak structure, as illustrated in Figure 40(b), the G-band spectra of misoriented bi-layer graphene shows a one-peak profile, with an upshift of $\sim 14\,\text{cm}^{-1}$. This result is generally consistent with the observations for turbostratic graphite shown in Figure 40 and it was explained as due to changes in the Fermi velocity of graphene due to interlayer interactions in AB-stacked samples [295]. These aspects also explain why a broadened single G′ peak is observed for regions of a sample that contains domains of mono-layer or bi-layer graphene. For example, CVD-grown graphene often shows such domains of mono-layer and bi-layer graphene and furthermore the stacking of the layers is often not AB Bernal stacking [85,305,306]. Using a similar path of reasoning as was followed to understand the difference in the G′-band lineshape between mono-layer graphene and bi-layer graphene with AB stacking, it is easy to understand that the G′ lineshape will be different for ABC and ABA trilayer graphene stacking. Recently, Liu *et al.* [307] showed that the G′-band can indeed be used to distinguish between ABC versus ABA stacking in trilayer graphene samples. The G′-band for ABC stacked samples is generally broader than that for ABA, and by mapping the G′ width, Liu *et al.* showed that these two types of stacking order coexist in trilayer graphene samples. By mapping several samples, they showed that about 15% of the samples generated by the mechanical exfoliation of HOPG are ABC-stacking-like, and this value for the mixed stacking order is in very good agreement with X-ray studies on HOPG [9].

4.3. *D-band and G-band intensity ratio and other disorder effects*

Graphene provides an ideal structure to study the effect of disorder on a Raman spectrum, because in a mono-layer 2D structure one does not have to worry about cascade effects and the penetration depth of the light [3,65,292]. Here we discuss the effect of disorder caused by low energy Ar^+ bombardment [3].

4.3.1. *Ar^+ ion bombardment on graphene*

Raman spectroscopy is one of the most sensitive techniques that can be used to characterize disorder in the sp^2 network of carbon materials [308]. It is widely used to identify disorder in diamond-like carbon, amorphous carbon, nanostructured carbon, carbon nanofibers, carbon nanotubes and carbon nanohorns [2,174]. Just as Raman spectroscopy has been used for the characterization of defects through the observation of symmetry-breaking features in the Raman spectra, point defects have been used as a characteristic defect that can be readily reproduced [308] and the uses of ion implantation to create these point defects has been widely adopted.

The first-order Raman spectra of crystalline graphene is shown in Figure 42(a), where the presence of the Raman-allowed G-band is observed. When graphene is bombarded by Ar^+ ions (starting with a low dose, $10^{11}\ \text{Ar}^+/\text{cm}^2$ in Figure 42(b)), point defects are formed and the Raman spectra of the disordered graphene exhibit two new sharp features, named by D and D′, appearing at $1345\,\text{cm}^{-1}$ and $1626\,\text{cm}^{-1}$, respectively, for $E_{\text{laser}} = 2.41\,\text{eV}$ (Figure 42(b)). The D and D′ labels indicate that these Raman bands are induced by disorder [102]. Both of these bands are dispersive and change frequency when changing $E_{\text{laser}} = 2.41\,\text{eV}$. Actually, the DR process discussed for the symmetry-allowed G′-band was developed to explain the dispersive behavior of the D-band [104]. Instead of electron scattering by two phonons with momentum q and $-q$, the breaking of the translational symmetry of crystals can be activated by introducing defects into the lattice. Introducing disorder breaks down the momentum conservation requirement, and phonons at interior *k* points of the BZ can contribute to the Raman scattering process. Similar to the case of the G′-band, those scattering processes due to point defects which fulfill the DR process are privileged in the disorder-induced Raman scattering process discussed in this section.

Finally, if the periodic structure of graphene is largely disordered, for example from a high defect density caused by applying a large ion dose bombardment, such as 10^{15} Ar^+/cm^2, the Raman spectrum evolves into a phonon DOS-like profile, where most of the higher-energy optical phonon branch would be contributing to the spectra, rather than solely the special phonons fulfilling the DR process (see Figure 42(c)) [3]. Of course in a fully disordered material, not only are all phonons activated, but also changes in the structure, bonding and strain fields change the vibrational frequencies and lineshapes.

4.3.2. *The D to G intensity ratio and the L_D dependence*

Mono-layer graphene samples were bombarded with Ar^+ ions and consecutive Raman spectra were performed to study the evolution of the disorder-induced Raman peaks [3]. Figure 43 shows the Raman spectra of a graphene mono-layer sample subjected to the ion bombardment procedure that is described in the beginning of Section 4.3.5. From the pristine sample (bottom spectrum in Figure 43) to the lowest bombardment dose in Figure 43 (10^{11} Ar^+/cm^2), the D-band process is activated, showing a very small D-band intensity relative to the G peak which is symmetry-allowed. Within the bombardment dose range 10^{11}-10^{13} Ar^+/cm^2, the intensities of the disorder induced peaks increase. A second disorder-induced peak around ~1620 cm^{-1} (the D′-band) also becomes clearly evident at a dose of 10^{12} Ar^+/cm^2, but we do not focus on this feature here. The Raman spectra start to broaden significantly above 10^{13} Ar^+/cm^2, and the spectra end up exhibiting the graphene phonon density of states-like spectrum, corresponding to Figure 42(c)). From 10^{14} Ar^+/cm^2 (top spectrum in Figure 43) and above, the Raman scattering shows a lineshape broadening with no measurable change in the peak frequencies of these broad features.

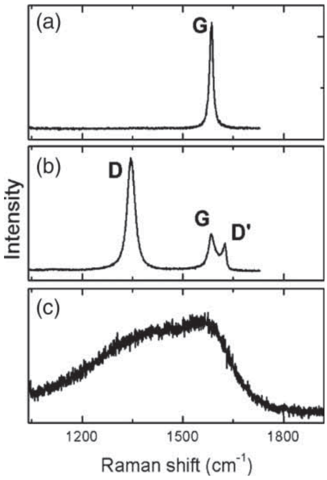

Figure 42. The Raman spectrum of (a) crystalline graphene, (b) defective graphene, (c) and fully disordered single-layer graphene. These spectra were obtained with $E_{laser} = 2.41$ eV and the graphenes are deposited on a SiO_2 substrate using the mechanical exfoliation method (scotch-tape). Reprinted with permission from A. Jorio *et al.*, Journal of Physics: Condensed Matter 22, p. 334204, 2010 [309]. Copyright © (2010) by the Institute of Physics.

The development of disorder in sp^2 carbon nano-crystallites is conveniently described by plotting the I_D/I_G ratio as a function of crystallite size [102]. Here we perform a similar analysis, but plotting the I_D/I_G ratio as a function of the average distance L_D between defects, as shown in Figure 44. Note that the I_D/I_G ratio has a non-monotonic dependence on L_D. The I_D/I_G ratio is here seen to increase initially with increasing L_D, up to $L_D \sim 3.5$ nm, and then it decreases for $L_D > 3.5$ nm, consistent with the proposed amorphization trajectory for sp^2 carbon nano-crystallites [131]. Such a behavior indicates the existence of two competing mechanisms that contribute to the Raman D-band, as described below.

4.3.3. *The D to G intensity ratio: the "local activation" model*

The impact of a single ion on a graphene sheet causes modifications on two length scales, which we denote here by r_A and r_S. These two length scales represent, respectively, the radii of two circular areas measured from the impact point, as shown in Figure 45. Structural disorder from the impact position occurs within the shorter radius r_S, where the subscript S stands for structurally disordered. For distances larger than r_S but shorter than r_A, the lattice structure is preserved but a break-down of the selection rule is caused by the proximity to the structurally disordered area (S-region), thus leading to a local enhancement of the Raman D-band. We call this the A-region, where A stands for activated. When the Raman scattering process occurs at distances larger than $\ell_\phi = r_A - r_S$ from the defective region, only the G-band is active. The I_D/I_G ratio is then given as a function of the average distance between two defects, L_D, by [3]:

$$\frac{I_D}{I_G}(L_D) \propto I_D(L_D) = C_A f_A(L_D) + C_S f_S(L_D). \tag{73}$$

The intensity I_G remains constant, independent of L_D, while f_A and f_S are the fractions of the A and S areas in the sheet, respectively, with respect to the total area. Both the A and S regions break momentum conservation and give rise to a D-band. However, the A-regions will contribute

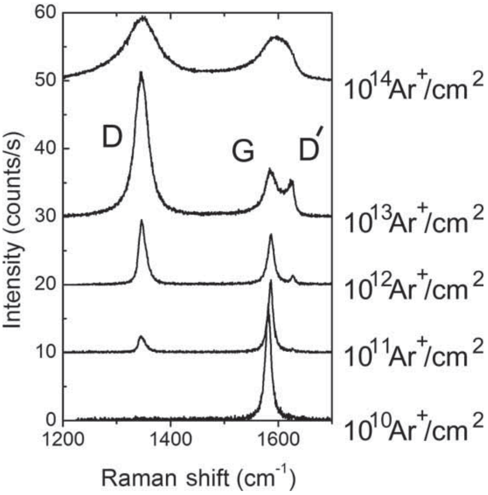

Figure 43. Evolution of the first-order Raman spectra using a $\lambda = 514$ nm laser ($E_{\text{laser}} = 2.41$ eV) to investigate a graphene mono-layer sample deposited on an SiO$_2$ substrate, and subjected to Ar$^+$ ion bombardment. The Ar$^+$ ion doses from the bottom trace to the top trace are: zero (pristine), 10^{11}, 10^{12}, 10^{13} and 10^{14} Ar$^+$/cm^2 for 90 eV ions. The spectra in this figure are also displaced vertically for clarity. Reprinted From Carbon 48(5), M.M. Lucchese *et al.*, pp. 1592–1597 [3]. Copyright © (2010) Elsevier.

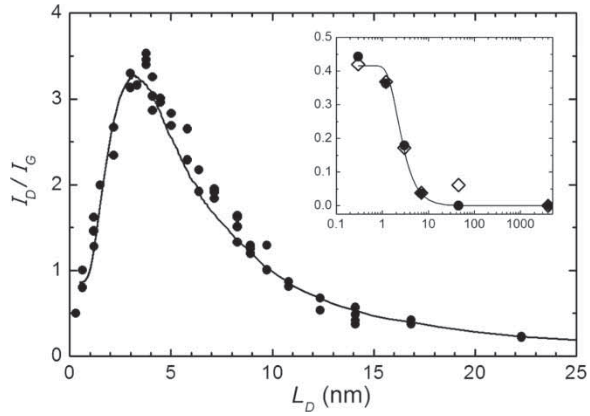

Figure 44. The I_D/I_G data points from three different mono-layer graphene samples as a function of the average distance L_D between defects, induced by the Ar$^+$ ion bombardment procedure described in Section 4.3.2. The solid line is a modeling of the experimental data with Equation (73). The inset shows a plot of I_D/I_G vs. L_D on a log scale for two samples: (i) a ∼50-layer graphene sample; (ii) a 2 mm-thick HOPG sample, whose measured values are here scaled by $(I_D/I_G) \times 3.5$. Reprinted From Carbon 48(5), M.M. Lucchese *et al.*, pp. 1592–1597 [3]. Copyright © (2010) Elsevier.

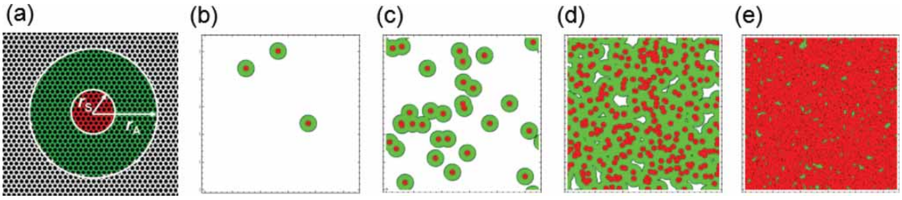

Figure 45. (a) Definition of the “activated” A-region (darkest gray) and “structurally disordered” S-region (dark gray). The radii r_S and r_A are measured from the impact point which is chosen randomly in this simulation. (b–e) show 55 nm × 55 nm portions of the graphene simulation cell, with snapshots of the structural evolution of the graphene sheet for different defect concentrations: (b) 10^{11} Ar$^+$/cm^2; (c) 10^{12} Ar$^+$/cm^2; (d) 10^{13} Ar$^+$/cm^2 and (e) 10^{14} Ar$^+$/cm^2, as in Figure 43. Reprinted From Carbon 48(5), M.M. Lucchese *et al.*, pp. 1592–1597 [3]. Copyright © (2010) Elsevier.

most strongly to the D-band, while the S-regions will make less contribution to the D-band due to the break-down of the lattice structure itself. These two different scattering cross sections for the disorder-induced processes will give rise to the non-monotonic behavior observed in the L_D dependence of the I_D/I_G ratio, as shown in Figure 44.

The structurally disordered (S) region and the activated (A) region are shown in Figure 45(a) by light and dark gray regions, respectively. The evolution of the S and A regions for a graphene sheet under ion bombardment was simulated by randomly choosing a sequence of impact positions on a graphene sheet. As the number of impacts increase, the activated A-region increases, leading to a decrease in L_D and an increase of the D-band intensity I_D. When the graphene is fully covered with A-regions, an increase in ion bombardment fluence causes the structurally disordered S-regions to take over from the A-regions, thus leading to a decrease of the D-band intensity I_D (see Figure 45(b–e)). This model is the basis for the evolution of I_D/I_G based on Equation (73) which, with the parameters $C_A = 4.56$, $C_S = 0.86$, $r_A = 3$ nm and $r_S = 1$ nm, give the line curve in Figure 44 that fully describes the experimental evolution of I_D/I_G, shown by the black bullets in Figure 44 [3].

For low defect concentrations (large L_D values), $I_D/I_G = (102 \pm 2)/L_D^2$, which means the total area contributing to scattering is proportional to the number of defects. This regime is valid for $L_D > 2r_A$, while below this limit for L_D, the activated regions start to overlap (see Figure 45(e)), thus changing the simple $I_D/I_G \propto L_D^{-2}$ dependence. The D-band intensity then reaches a maximum and a further increase in the defect concentration decreases the D-band intensity because the graphene sheet starts to be dominated by the structurally disordered areas (S-region).

The $r_S = 1\,\text{nm}$ value is in agreement with the average size of the disordered structures seen in the STM images [3,130]. This is not a universal parameter, but is a parameter that is actually specific to the ion bombardment process. The $\ell_\phi = r_A - r_S = 2\,\text{nm}$ value represents the Raman relaxation length for the defect-induced resonant Raman scattering in graphene. This value is valid for the laser excitation energy 2.41 eV and room temperature, and may change with changing E_{laser} and temperature. Be aware that this is the relaxation length for the excited electrons, which should not be confused with the relaxation length for the phonons. The value $C_A = 4.56$ is in rough agreement with the ratio between the electron–phonon coupling for the iTO phonons evaluated between the Γ and the K points in the BZ [218–220], which is consistent with the expectation that the C_A parameter should be related to the electron–phonon matrix elements. The C_S parameter is related to the size of the highly disordered area, and there is no theoretical work yet available on this matter.

It is important to have an equation relating I_D/I_G to L_D that can be used by researchers looking for a Raman characterization of the defect density present in a specific graphene sample. The entire regime ($0 \to L_D \to \infty$) can be fitted using [3]:

$$\frac{I_D}{I_G} = C_A \frac{r_A^2 - r_S^2}{r_A^2 - 2r_S^2}\left[\exp\left(\frac{-\pi r_S^2}{L_D^2}\right) - \exp\left(\frac{-\pi (r_A^2 - r_S^2)}{L_D^2}\right)\right] + C_S\left[1 - \left(\frac{-\pi r_S^2}{L_D^2}\right)\right], \qquad (74)$$

which comes from solving rate equations for the bombardment process. Fitting the data in Figure 44 with Equation (74) gives $C_A = (4.2 \pm 0.1)$, $C_S = (0.87 \pm 0.05)$, $r_A = (3.00 \pm 0.03)\,\text{nm}$ and $r_S = (1.00 \pm 0.04)\,\text{nm}$. This equation represent the results very well, since the fitting obtained with Equation (74) is also in very good agreement with experiment and the fitting parameters are fully consistent with the parameters obtained by computational modeling using Equation (73) [3].

4.3.4. *The Local Activation Model and the Raman Integrated Areas*

The dependence of the intensity ratio I_D/I_G on L_D was found to accurately follow an analytical formula (Equation (74)), as described above, and this result is useful for practical applications and for inter-laboratory comparisons. However, the physics behind this effect has to take into account that both I_D and I_G vary when L_D is changed. As discussed in Section 1.4.5, the evolution of the Raman profile can be discussed as related to the peak intensity or to the integrated peak area. In this section, we choose to use the same model as was used to derive Equation (74) when we analyze the evolution of the intensity and integrated area of the many Raman peaks that vary with increasing structural disorder, by normalizing each of them to the G-band integrated area (see Figure 46). As shown in the inset to Figure 46 (top-right panel), the integrated area of the G-band does not show any simple evolution with disorder [130].

The lower-left panels of Figure 46 show that this analytical expression fits the quantities A_D/A_G and $A_{D'}/A_G$ nearly perfectly, where A refers to the integrated area. For the D-band, the fitting parameters are $r_S = 2.6\,\text{nm}$, $r_A = 4.1\,\text{nm}$, $C_S = 2.4$ and $C_A = 3.6$, whereas for the D′-band the fitting parameters are $r_S = 2.6\,\text{nm}$, $r_A = 3.8\,\text{nm}$, $C_S = 0.28$ and $C_A = 0.19$. Note that we obtain close to the same value of r_S for both the D and D′ modes, indicating that indeed r_S

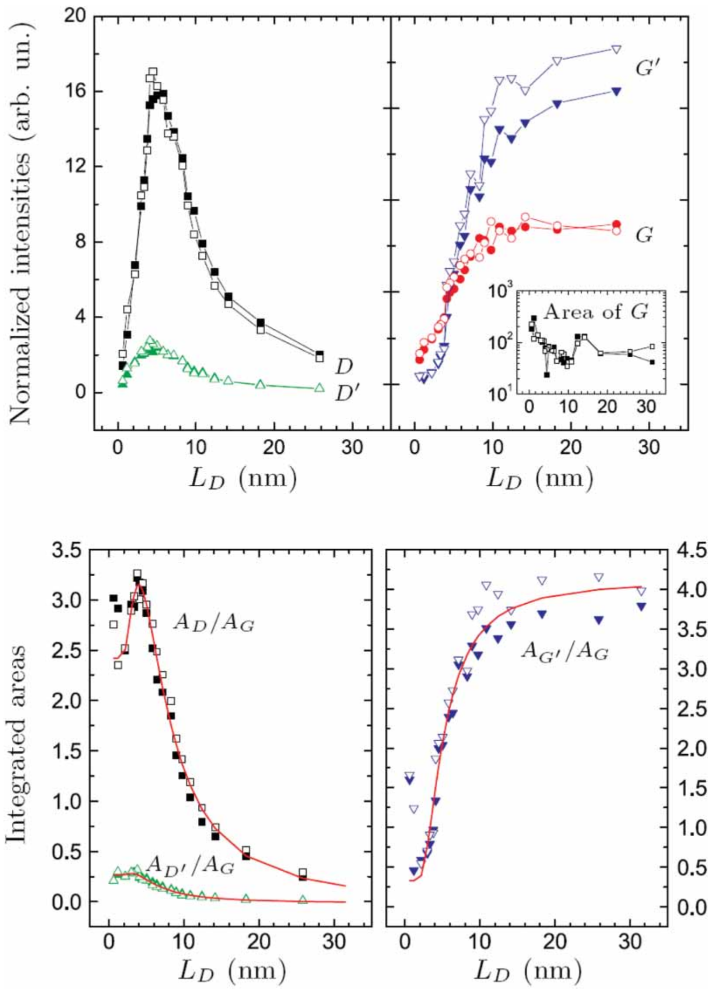

Figure 46. Normalized intensities (upper panel) and areas (lower panel) of the Raman D-, D′-, G- and G′-bands as a function of L_D. All quantities are normalized by the area of the G-band (see the as-measured A_G in the inset to the upper-right panel). The solid lines in the lower panel are theoretical results based on the model described in Section 4.3.4. Reprinted figure with permission from E.H. Martins Ferreira *et al.*, Physical Review B 82, p. 125429, 2010 [130]. Copyright © (2010) by the American Physical Society.

is a geometrical, structure-related length. Also, we find 1.5 and 1.3 nm for the spatial extent of the Raman processes $r_A - r_S$, which is of the same order of magnitude as the rough estimates $v_F/\omega_D = 4.3$ nm and $v_F/\omega_{D'} = 3.6$ nm. We remind the reader that the distance $r_A - r_S$ is a rough measure of the length traveled over the lifetime of the e–h pair, v_F/ω_X, where v_F is the graphene Fermi velocity of the electron and hole carriers and ω_X is the frequency of any X phonon mode [130]. More interestingly, the ratio between $r_A - r_S$ for the D- and D′-bands matches very closely to the ratio of the inverse frequencies $\omega_{D'}/\omega_D \approx 1.2$.

Similar ideas can be applied to a discussion of the $A_{G'}/A_G$ ratio, but in this case, since the G′-band is already active for pristine graphene, the intensity ratio is only affected by the disruption of the hexagonal network, leading to a decrease in the $A_{G'}/A_G$ ratio as a function of increasing disorder described by the simple formula [130]

$$\frac{A_{\mathrm{G}'}}{A_{\mathrm{G}}}(L_{\mathrm{D}}) = \frac{A_{\mathrm{G}'}}{A_{\mathrm{G}}}(\infty) - B\left[1 - \exp\left(-\frac{\pi r_{\mathrm{S}}^2}{L_{\mathrm{D}}^2}\right)\right], \tag{75}$$

where $A_{\mathrm{G}'}/A_{\mathrm{G}}(\infty)$ is the area ratio for pristine graphene while $A_{\mathrm{G}'}/A_{\mathrm{G}}(L_{\mathrm{D}})$ is the area ratio for an actual sample characterized by its L_{D} value. The fitting of the experimental data, shown in the lower-right panel of Figure 46, gives in this case $r_{\mathrm{S}} = 2.5$ nm, which is also similar to the structural damage length obtained for the D- and D′-band spectra. This result is in accordance with the typical defect-size estimates found independently from the STM analysis [3,130]. In Section 4.3.5, we describe what happens to the frequency and linewidth of the Raman peaks as a result of ion implantation-induced structural damage.

4.3.5. *Modeling disorder effects in the Raman linewidths and frequency shifts: the spatial correlation model for defects*

Disorder introduced by a random distribution of defects causes a broadening and a shifting of the Raman mode frequencies and increases in the asymmetry of both the Raman-allowed and the newly disorder-activated Raman bands discussed in Section 4.3.4. Here, we use the so-called "spatial-correlation model" introduced by Capaz and Moutinho in [130] to describe these effects in graphene. Other work on this topic that should also be referred to is in Refs. [65,292],

As described in Section 1.4.6, a random distribution of point defects will scatter phonons and it will also add a contribution to the FWHM by an el–ph coupling of phonons with wave vectors $\mathbf{q}_0$ and $\mathbf{q}_0 + \delta\mathbf{q}$. In the limit of low levels of disorder, the Raman intensity for the disordered graphene $I(\omega)$ can be calculated by Equation (7). With this model, we can calculate the full lineshape of $I(\omega)$ and from that we can extract the disorder-induced peak shifts $\Delta\omega_{\mathbf{q}_0}$ (Figure 47, lower panel) and the increases in the FWHM $\Delta\Gamma_{\mathbf{q}_0}$ (Figure 48, lower panel). Since we use experimentally available dispersion relations $\omega(\mathbf{q})$, the only fitting elements in this model are: (1) the relationship between the coherence length L and the typical inter-defect distance L_{D}, and (2) the weighting function $W(\mathbf{q})$ in Equation (7).

We now describe in more detail the application of the above model to the different Raman bands considered in graphene, including the G-band, the D′-band, the D-band and the G′-band [130].

A. G-*band* – The G-band in perfect graphene is associated with phonons at the Γ-point, i.e., $\mathbf{q}_0 = 0$ phonons. We consider that disorder mixes equally the Γ-point phonons with nearby phonons in both the LO and iTO phonon branches. We find that the best agreement with experiment is obtained by using a constant weighting function (which is equivalent to not use a weighting function at all). For the LO and TO phonon dispersions, we take

$$\begin{aligned} \omega_{\mathrm{LO}}(q) &= \omega_{\mathrm{G}} + 181q - 230.29q^2, \\ \omega_{\mathrm{iTO}}(q) &= \omega_{\mathrm{G}} - 135.42q, \end{aligned} \tag{76}$$

where $\omega_n(q)$ is in cm^{-1} (n = LO or iTO) and $\omega_{\mathrm{G}} = 1580$ cm^{-1} is the experimental G-band frequency for pristine graphene used in this work. Here q is measured from the Γ-point in units of Å^{-1}. These dispersions are taken from the work of Maultzsch *et al.* [208] by interpolating the frequencies at high-symmetry points and by averaging the dispersions between the Γ–K and Γ–M directions. Also, since the main contribution to the integral in Equation (7) will come from q vectors near the Γ point, the BZ can be safely approximated by a circular disk and the integral will be considered explicitly in the radial coordinate only. Taking all these considerations into account, Equation (7)

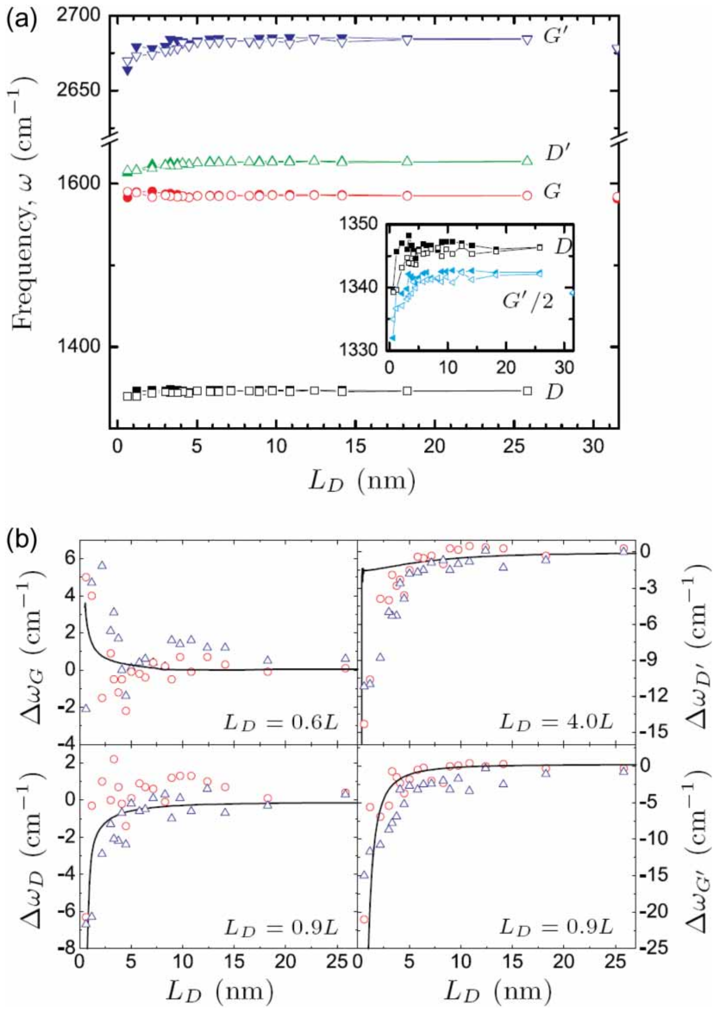

Figure 47. The upper panel shows peak frequencies of the D, G, D′ and G′-bands as a function of L_D denoting a typical distance between defects. The inset compares the frequency of the D-band and the G′-band divided by two, showing that we always have $\omega_{\mathrm{G}'}/2 < \omega_D$, in agreement wtih Ref. [216]. The lower panel shows frequency shifts with respect to the zero-disorder limit. Dots are experimental points and solid lines are theoretical results based on the model described in the text. Experimental error bars are 2 cm^{-1}. Reprinted figure with permission from E.H. Martins Ferreira *et al.*, Physical Review B 82, p. 125429, 2010 [130]. Copyright © (2010) by the American Physical Society.

becomes [130]

$$I_\mathrm{G}(\omega) \propto \sum_n \int 2\pi q \mathrm{d}q \frac{\exp[-q^2L^2/4]}{[\omega - \omega_n(q)]^2 + [\Gamma_0/2]^2} \tag{77}$$

in which the sum is over the two (LO and iTO) phonon branches.

B. D′*-band* – The D′-band arises from intra-valley phonons with a linear wavevector intensity dependence with respect to the laser energy. Since the D′-band has been assigned to LO phonons, only this branch is considered in calculations of the D′-band intensity using Equation (7). We

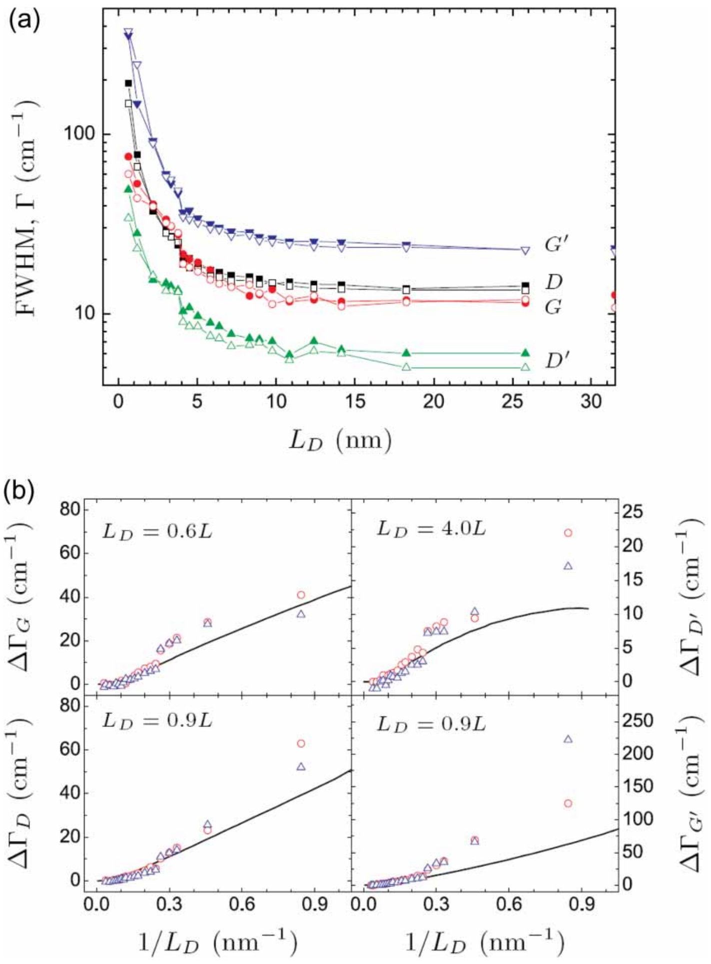

Figure 48. (a) FWHM intensity of the D-, G-, D′- and G′-bands as a function of L_D, denoting the typical distance between defects. (b) Disorder contribution to the peak widths, ΔΓ, for the D, G, D′ and G′-bands. Points denote are experiments and solid lines are theoretical results based on the model described in the text. Reprinted figure with permission from E.H. Martins Ferreira *et al.*, Physical Review B 82, p. 125429, 2010 [130]. Copyright © (2010) by the American Physical Society.

average over all possible directions θ of the wavevector $\mathbf{q}_0$ and, similarly to the case of the G-band, there is no need to introduce a q-dependent weighing function $W(\mathbf{q})$. Then, the D′-band intensity becomes [130]:

$$I_{D'}(\omega) \propto \int q\mathrm{d}q\,\mathrm{d}\theta \frac{\exp[-(\mathbf{q}-\mathbf{q}_0)^2 L^2/4]}{[\omega-\omega_{\mathrm{LO}}(q)]^2+[\Gamma_0/2]^2}. \tag{78}$$

For the laser energy of 2.41 eV, the value for $|\mathbf{q}_0|$ in Equation (78) is found to be $|\mathbf{q}_0| = 0.42\,\text{Å}^{-1}$ measured from the Γ point.

C. D-band – The D-band arises from inter-valley phonons which also show a linear wavevector dependence with respect to the laser energy. In fact, for the laser energy of 2.41 eV, we also find $|\mathbf{q}_0| = 0.42\,\text{Å}^{-1}$ for the D-band, but now $\mathbf{q}_0$ is measured from the K point. Since the D-band has been assigned to iTO phonons along the K–M direction in the BZ, we choose $\mathbf{q}_0$ along this direction and the weighting function $W(\mathbf{q})$ is also restricted to be non-zero only along the same direction. Mathematically, $W(\mathbf{q}) = \delta(\theta - \theta_{\mathrm{K-M}}) f(q)$, where $\theta_{\mathrm{K-M}}$ indicates the *K–M* direction and $f(q) = 1 + a(q_0 - q)$ is a function that linearizes the radial dependence of the electron–phonon coupling along the *K–M* direction near q_0. With these conditions, the D-band intensity becomes [130]

$$I_{\mathrm{D}}(\omega) \propto \int \mathrm{d}q \frac{f(q)\exp[-(q-q_0)^2 L^2/4]}{[\omega - \omega_{\mathrm{iTO}}(q)]^2 + [\Gamma_0/2]^2}. \tag{79}$$

For the iTO phonon dispersion along the *K–M* direction, we use [244]:

$$\omega_{\mathrm{iTO}}(q) = \omega_K + 589.35q - 485.46q^2, \tag{80}$$

where ω_{iTO} is in cm^{-1} and q is measured from the K point in units of Å^{-1}.

D. G′-*band* – The G′-band is related to a DR process associated with the same inter-valley phonons as the D-band. For this reason, the expression for the intensity becomes more complicated and it involves a double integral over the forward (q) and backward (q') phonon wavevectors. Using the same considerations for the el–ph matrix elements, which essentially select phonons in the *K–M* direction, we have

$$I_{\mathrm{G'}}(\omega) \propto \int \mathrm{d}q\,\mathrm{d}q' \frac{f(q)f(q')\exp\left[(-[(q-q_0)^2 + (q'-q_0)^2]L^2)/4\right]}{[\omega - \omega_{\mathrm{iTO}}(q) - \omega_{\mathrm{iTO}}(q')]^2 + [\Gamma_0/2]^2} \tag{81}$$

where $f(q)$ is the same linear function as in the D-band case and q_0 is also the same. We also impose the condition that the same relation between L (the disorder-induced phonon coherence length) and L_{D} (the average distance between defects) must be valid for the D and G′-bands.

In Figures 47 and 48, we see the results for the frequency and linewidth as a function of the typical distance L_{D} between defects for the data fitting of the frequency shifts and widths, respectively, as described above. Note that the general agreement is good, especially for large values of L_{D}. Indeed, this spatial correlation model, because of its perturbation character, is not expected to be valid in the highly disordered regime. In Figures 47 and 48, the best relationships between L and L_{D} in each case are shown (as obtained by the fits between the model and the experimental data). It is physically reasonable to see that L and L_{D} are similar to each other. This condition was not imposed, but it comes automatically from the fitting procedure. This means that the disordered-induced phonon coherence length L is of the same order of magnitude as the typical inter-defect distance L_{D}, which is physically reasonable. There is no reason to expect that the same relation between L and L_{D} should be found for the different phonon modes, since different modes should have different defect scattering cross-sections. From the results shown here, it seems that the D′ modes are the most affected by point defect disorder, showing a smaller coherence length than the other modes for the same amount of disorder. Finally, the model allows us to explain the greater increase in the FWHM for each of the modes near the K point relative to the modes near the Γ point as being simply a consequence of the larger magnitude of the phonon dispersions near the K point.

4.3.6. *Evolution of overtone and combination modes*

In Figure 49, we present the spectral evolution of the G′-band and other second-order processes in mono-layer graphene for three different ion dose levels. The G′ and G″-band intensities decrease as the line widths increase for increasing ion dose. The defect-related combination modes D + *G* at 2930 cm^{-1} and G + *D*′ at 3190 cm^{-1} can be observed at higher ion bombardment doses (10^{13} Ar$^+$/cm^2), but the G″-band is too weak to be seen in these measurements. At a dose of

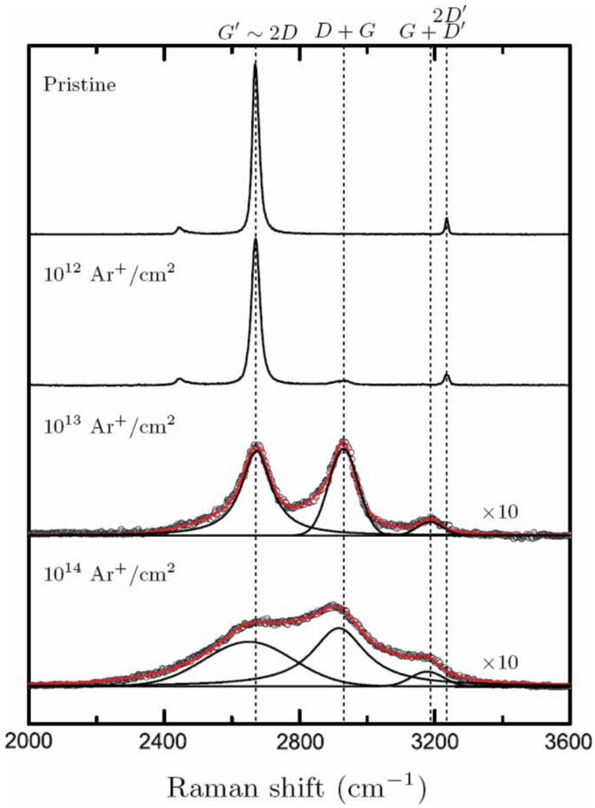

Figure 49. Evolution of the G′-band (at 2670 cm^{-1}) and other second-order peaks, the (D + G) at 2930 cm^{-1}, the (D′ + G) at 3190 cm^{-1}, and the G'' ($2D'$ in the figure) at 3220 cm^{-1} with increasing ion doses. The intensities of the two lower graphs are multiplied by a factor of 10 for the sake of readability [130]. Here the notation $2D'$ is used instead of G″, as has also been used in the literature by other authors. Reprinted figure with permission from E.H. Martins Ferreira *et al.*, Physical Review B 82, p. 125429, 2010 [130]. Copyright © (2010) by the American Physical Society.

10^{14} Ar$^+$/cm^2 the results show a frequency downshift for all DR features, in agreement with the results of Section 4.3.5.

4.3.7. *Disorder and the number of layers*

The I_D/I_G results for ion bombarded graphene depend on the number of graphene layers N [130] in the case of low energy ions (90 eV). Because of the low ion energy, the ion bombardment process is limited generally to one defect per bombarding ion, so that the I_D/I_G scales with N. For many-layer graphene (∼ 50 and higher), a monotonic evolution of I_D/I_G with increasing ion fluence is seen because in this case there are always more unperturbed graphene layers available to be bombarded.

4.4. *Edge phonon Raman spectroscopy*

The disorder-induced Raman bands should also depend on the type of defect structure, and not only on the number of defects. This dependence has been demonstrated for graphene and graphite edges, where the orientation of the carbon hexagons with respect to the edge axis was determined experimentally, thereby distinguishing the so-called zigzag edge from the armchair or random atomic edge structures [170]. The armchair/random vs. zigzag edge structure can be identified spectroscopically by the presence vs. absence of the D-band, and this effect results from the momentum requirements of the DR model, as discussed below.

The defect associated with a step edge has a 1D character, which means that it is able to transfer momentum solely in the direction perpendicular to the edge. In this sense, the wave vectors of the defects associated with zigzag and armchair edges are represented in Figure 50(a) by $\vec{\mathbf{d}}_a$ (a for armchair) and $\vec{\mathbf{d}}_z$ (z for zigzag) edges. When we translate these vectors into reciprocal space, we see that different selection rules apply for the electron scattering by phonons for each of these edge types. This is illustrated in Figure 50(b), where the first BZ of 2D graphite (graphene) is shown, oriented in accordance with the real space directions shown in Figure 50(a).

Light-induced e–h pairs will be created on an equi-energy circle around points K' and K (here neglecting the trigonal warping effect for simplicity), which has a radius that is defined by E_{laser}, as shown in Figure 50(b). Note that for inter-valley electron-defect scattering, which connects K to K' points, only the $\vec{\mathbf{d}}_a$ vector for armchair edges can connect points belonging to circles centered at two inequivalent K and K' points. In contrast the zigzag $\vec{\mathbf{d}}_z$ vector to connect inequivalent points, which means that inter-valley scattering is not allowed for zigzag edges. This therefore means that the inter-valley DR process, which is the process responsible for the observation of the D-band in graphitic materials, is not allowed for a perfect zigzag edge [170]. The D-band phonon connects two inequivalent K and K' points, and along the zigzag edge there will be no defect able to connect those points to achieve momentum conservation in the final process.

On the other hand, intra-valley electron-defect scattering can occur for both zigzag and armchair edges (see Figure 50(b)). Therefore, intra-valley scattering processes induced by phonons can achieve final momentum conservation using both $\vec{\mathbf{d}}_a$ and $\vec{\mathbf{d}}_z$ vectors. Another well-known defect-induced band is the so-called the D′-band, which appears at around 1620 cm^{-1}, and it is related to intra-valley el–ph processes. For this reason, the D′-band observation should be independent of the zigzag vs. armchair structure of the edges, in agreement with experimental observation.

Another selection rule aspect refers to the D-band intensity dependence on the polarization direction of the light with respect to the edge orientation. The D-band intensity has a maximum value when the light is polarized along the edge, and should give a null value when the light is polarized perpendicular to the edge. The physics behind this selection rule is the optical absorption (emission) anisotropy around the $K(K')$ point in 2D graphite, which can be represented by [262]

$$W_{\text{abs,ems}} \propto |\vec{P} \times \vec{k}|^2. \tag{82}$$

Here the polarization of the incident (scattered) light for the absorption (emission) process is represented by $\vec{P}$, while the wave vector of the electron measured from the K point is given by $\vec{k}$.

These selection rules were first observed for graphite edges, as reported in [170], and similar results have been observed later in mono-layer graphene [151,311]. However, only edge-dependent variations in the D-band intensity consistent with the selection rules have been reported. Raman-based indications for the high crystallinity of zigzag edges have indeed been observed by Krauss *et al.* [312], although the complete absence of the D-band together with the observation of the D′-band, which is expected for a zigzag edge structure, has never been reported, which might imply that, up to now, no perfect zigzag structure has been measured by Raman spectroscopy. In general, the polarization direction dependence for the D-band intensity, as given by Equation (82), together with the zigzag vs. armchair dependence, can be used for an identification of the edge orientation and structure. Raman spectroscopy is, therefore, a valuable tool for the development of our understanding of edge structures, important for the science of graphene ribbons, and more. The results reported here represent an effort to improve our understanding of the influence of